Energy transfer of hypersonic and high-enthalpy boundary layer instabilities and transition

Xianliang Chen, Liang Wang, and Song Fu*

School of Aerospace Engineering, Tsinghua University, Beijing 100084, China

(Received 11 August 2021; accepted 10 February 2022; published 8 March 2022)

In this study, the disturbance energy budget is analyzed on the derived disturbance energy norm in hypersonic and high-enthalpy boundary layers with thermal-chemical nonequilibrium (TCNE) effects. The disturbance growth rate is decomposed to quantitatively evaluate the contribution from various classified terms. Hypersonic flat-plate flows are investigated with various free-stream Mach numbers, free-stream temperatures, and wall temperatures. The linear and nonlinear evolutions of disturbances are predicted using linear stability theory and parabolized stability equations. The results show that in the first-mode region, the disturbance growth rates are determined by the production term (destabilizing) and the viscous term (stabilizing), while the former nearly offset the latter. In the second-mode region, the viscous term decreases to the minimum, resulting in the dominance of the second mode. The disturbance of the TCNE source term has a stabilizing effect on the second mode, but at most it reduces the growth rate by 6% in a Mach 10 adiabatic case with the highest free-stream temperature of 900 K. The production term is mainly responsible for the second-mode growth rate difference between the TCNE flow and calorically perfect gas flow. TCNE changes the disturbance characteristics mainly through the mean flow modification. In the oblique-mode breakdown case, the intensive energy transfer between the selected modes and their harmonic waves is found to occur where they interact strongly with the mean flow.

DOI: 10.1103/PhysRevFluids.7.033901

I. INTRODUCTION

Accurate prediction and effective control of the hypersonic boundary layer transition from laminar to turbulence are crucial to the design of thermal protection systems and engine intake of high-speed vehicles. However, this problem is still unresolved because of the high nonlinearity and sensitivity in the transition process [1]. The flow transition is even more complicated in high-enthalpy boundary layers due to the existence of "high-temperature (real-gas) effects" [2]. Specifically, high temperature excites the vibrational and electronic energies within molecules and causes chemical dissociation and even ionization, all of which make the calorically perfect gas (CPG) assumption invalid. Instead, new physical models are required to describe the thermal-chemical nonequilibrium (TCNE) processes [3,4]. These high-temperature effects inevitably influence the boundary layer transition process.

A number of numerical techniques have been developed to study flow instabilities and transition in high-enthalpy boundary layers, including the linear stability theory (LST) [5], parabolized stability equations (PSEs) [6,7], secondary instability theory (SIT) [8], direct numerical simulation (DNS) [9,10], and so on. It was found that the second mode became destabilized at a higher frequency as the TCNE boundary layer became cooler and thinner. On the other hand, chemistry

*Corresponding author: fs-dem@mail.tsinghua.edu.cn

in the disturbances had a stabilizing or destabilizing effect depending on whether a reaction was endothermic or exothermic [11]. The use of Damköhler numbers, the ratio of the thermal-chemical timescales to the flow timescales, of the mean flow and the disturbance helps evaluate the effects of these two paths [12]. In addition to the second mode, the unstable supersonic mode, which appears downstream of the second-mode region, received much attention recently. Mortensen [13] found that the supersonic mode had a larger growth rate than the second mode on cones with large bluntness. Based on these linear results, the e^N method can be applied for the transition prediction. Miró Miró *et al.* [14] compared different physical models in detail to see their impact on the transition onset. In the nonlinear stage of the disturbance evolution, the fundamental resonance of the second mode was found to be dominant over the subharmonic one. The TCNE effects resulted in a higher maximum secondary growth rate and a larger corresponding spanwise wave number [7]. Besides, the chemical reactions were found not to influence the secondary growth directly, but indirectly affect through the change of the linear instability [15]. It can be seen that a great amount of work has been carried out to determine the most unstable modes and their growth rates. They are essential to identifying the dominant transition mechanisms in high-enthalpy boundary layers. Nevertheless, further research is required on the physical structures and energy transfer mechanisms in the disturbance evolution. Specifically, there are different terms in the governing equation for high-enthalpy flows, describing fluid convection, viscous dissipation, pressure diffusion, energy relaxation, species production/consumption, etc. It remains unclear the contributions of these terms in flow transition.

Energy budget analyses are effective ways to quantitatively evaluate the contributions from different terms and to investigate the energy transfer mechanisms in the disturbance growth. To derive the energy budget equation, disturbance energy requires to be defined in advance. For incompressible boundary layers, the disturbance energy is commonly taken as its kinetic energy, leading to the well-known Reynolds-Orr equation [16]. However, the definition is not unique for compressible, especially hypersonic boundary layers with the density and temperature disturbances of large amplitudes. Chu [17] derived a form of energy norm for CPG to include the contribution from all the disturbances of velocities, pressure (acoustic wave), and entropy (heat release). It was proved that in this form, the pressure-related transfer term in the energy-norm equation was eliminated so that the energy norm was monotonically nonincreasing in time in the absence of energy/force sources and other external energy inputs. In addition, this form was proven to lead to a self-adjoint system [18]. Because of its mathematical and physical foundations, this form of energy norm was widely adopted in the analyses for CPG of transient growth [19] and energy transfer mechanisms [20,21]. The resulting energy budget equation enabled a growth-rate decomposition to evaluate the contribution from each term in the governing equation to the disturbance growth [21,22].

In this work, the energy budget and transfer analyses are performed on the disturbance evolution, as predicted by LST and PSE, in hypersonic and high-enthalpy boundary layers with TCNE effects. The contributions from various terms in the governing equation to the disturbance growth are evaluated, and the energy transfer mechanisms are analyzed. This article is organized as follows. Section II provides the physical models as well as the formulations of PSE and energy-budget analyses. Section III gives the results of a benchmark case of Mach 10 flow over a flat plate. The cases with different mean flow parameters are studied in Sec. IV, and the nonlinear instability results are discussed in Sec. V. The work is summarized in Sec. VI.

II. PROBLEM FORMULATIONS

A. Governing equations

Ionization processes are usually negligible at a temperature lower than 9000 K. A good approximation of the five species model of air (N_2, O_2, NO, N, O) is considered in this work [2]. Extra conservation equations of species mass and vibrational energy are needed as compared with that for CPG flows [3]. The two-temperature model by Park [23] is employed, which consists of a translational/rotational temperature T and a vibrational temperature T_v. To provide the equations in the nondimensional form, the following relations of nondimensionalization are employed:

$$\begin{aligned}
&\boldsymbol{x} = \frac{\boldsymbol{x}^*}{L^*}, \quad t = \frac{t^* U_\infty^*}{L^*}, \quad \boldsymbol{u} = \frac{\boldsymbol{u}^*}{U_\infty^*}, \quad \rho = \frac{\rho^*}{\rho_\infty^*}, \quad T = \frac{T^*}{T_\infty^*}, \quad T_v = \frac{T_v^*}{T_\infty^*},\\
&p = \frac{p^*}{\rho_\infty^* U_\infty^{*2}}, \quad R_s = \frac{T_\infty^* R_s^*}{U_\infty^{*2}}, \quad c_{p,\mathrm{tr}} = \frac{c_{p,\mathrm{tr}}^*}{c_{p,\mathrm{tr},\infty}^*}, \quad h_s = \frac{h_s^*}{c_{p,\mathrm{tr},\infty}^* T_\infty^*}, \quad e_v = \frac{e_v^*}{c_{p,\mathrm{tr},\infty}^* T_\infty^*},\\
&\mu = \frac{\mu^*}{\mu_\infty^*}, \quad \kappa_{\mathrm{tr}} = \frac{\kappa_{\mathrm{tr}}^*}{\kappa_\infty^*}, \quad \kappa_v = \frac{\kappa_v^*}{\kappa_\infty^*}, \quad D_s = \frac{D_s^*}{D_\infty^*},\\
&\dot{\omega}_s = \frac{L^*}{\rho_\infty^* U_\infty^*}\dot{\omega}_s^*, \quad Q_{t-v} = \frac{L^*}{\rho_\infty^* U_\infty^*}\frac{Q_{t-v}^*}{c_{p,\mathrm{tr},\infty}^* T_\infty^*},
\end{aligned} \tag{1}$$

where the superscript $*$ denotes dimensional quantities, the subscript ∞ free-stream values, and L the reference length. The governing equations for TCNE flows are written as follows:

(i) *Continuity equation:*

$$\frac{\partial \rho}{\partial t} + \nabla \cdot (\rho \boldsymbol{u}) = 0 \tag{2a}$$

(ii) *Momentum equation:*

$$\rho\left(\frac{\partial \boldsymbol{u}}{\partial t} + \boldsymbol{u} \cdot \nabla \boldsymbol{u}\right) = -\nabla p + \nabla \cdot \left[\frac{\mu}{\mathrm{Re}_L}(\nabla \boldsymbol{u} + \nabla \boldsymbol{u}^{\mathrm{T}})\right] - \frac{2}{3}\nabla\left(\frac{\mu}{\mathrm{Re}_L}\nabla \cdot \boldsymbol{u}\right) \tag{2b}$$

(iii) *Translational/rotational energy equation:*

$$\begin{aligned}
&\rho c_{p,\mathrm{tr}}\left(\frac{\partial T}{\partial t} + \boldsymbol{u} \cdot \nabla T\right) - \mathrm{Ec}_\infty\left(\frac{\partial p}{\partial t} + \boldsymbol{u} \cdot \nabla p\right)\\
&= \frac{\mathrm{Ec}_\infty \mu}{\mathrm{Re}_L}\left[\nabla \boldsymbol{u} : (\nabla \boldsymbol{u} + \nabla \boldsymbol{u}^{\mathrm{T}}) - \frac{2}{3}(\nabla \cdot \boldsymbol{u})^2\right] + \nabla \cdot \left(\frac{\kappa_{\mathrm{tr}}}{\mathrm{Re}_L \mathrm{Pr}_\infty}\nabla T\right)\\
&\quad + \sum_m \left(\frac{\mu c_{p,\mathrm{tr},m}}{\mathrm{Re}_L \mathrm{Sc}_\infty}\nabla T \cdot \nabla Y_m\right) - Q_{t-v} - \sum_m (h_m \dot{\omega}_m)
\end{aligned} \tag{2c}$$

(iv) *Species continuity equation ($s \in [2, 5]$):*

$$\rho\left(\frac{\partial Y_s}{\partial t} + \boldsymbol{u} \cdot \nabla Y_s\right) = \nabla \cdot \left(\frac{\mu}{\mathrm{Re}_L \mathrm{Sc}_\infty}\nabla Y_s\right) + \dot{\omega}_s \tag{2d}$$

(v) *Vibrational energy equation:*

$$\rho c_{vib}\left(\frac{\partial T_v}{\partial t} + \boldsymbol{u} \cdot \nabla T_v\right) = \nabla \cdot \left(\frac{\kappa_v}{\mathrm{Re}_L \mathrm{Pr}_\infty}\nabla T_v\right) - \sum_m \left(\frac{\mu c_{vib,m}}{\mathrm{Re}_L \mathrm{Sc}_\infty}\nabla T_v \cdot \nabla Y_m\right) + Q_{t-v} \tag{2e}$$

(vi) *Equation of state:*

$$p = \rho T \sum_m (Y_m R_m). \tag{2f}$$

Here $\boldsymbol{u} = [u, v, w]^{\mathrm{T}}$ is the velocity vector, R_s the gas constant, $Y_s = \rho_s/\rho$ the mass fraction, h and e_v the specific enthalpy and vibrational energy, $c_{p,\mathrm{tr}}$ the translational-rotational component of the specific heat, and $c_{vib} = \partial e_v/\partial T_v$ the vibrational component. The transport properties, the mixture viscosity μ, thermal conductivity κ_{tr}, κ_v, and mass diffusion coefficient D_s, are calculated through the relations by Gupta *et al.* [24], which were shown to be as accurate as of the solution of the first-order Chapman-Enskog approximation in the absence of ions [25]. The collision cross sections between molecules are evaluated from the curve fits by Capitelli *et al.* [26]. The source terms Q_{t-v} and $\dot{\omega}_s$ are introduced to describe the energy relaxation process [27] and the finite-rate chemical reactions [28]. The chemical equilibrium constants are obtained from Gibbs energy fitted by McBride *et al.* [29]. For full details of the adopted TCNE models, one can refer to Ref. [30]. The dimensionless parameters in Eq. (2) are defined as follows:

$$\begin{aligned}
&\mathrm{Ma}_\infty = \frac{U_\infty^*}{a_{f,\infty}^*} = \frac{U_\infty^*}{\sqrt{\gamma_{f,\infty} R_\infty^* T_\infty^*}}, \quad \mathrm{Ec}_\infty = \frac{U_\infty^{*2}}{c_{p,\mathrm{tr},\infty}^* T_\infty^*} = (\gamma_{f,\infty} - 1)\mathrm{Ma}_\infty^2, \\
&\mathrm{Re}_L = \mathrm{Re}_\infty L^* = \frac{\rho_\infty^* U_\infty^* L^*}{\mu_\infty^*}, \quad \mathrm{Pr}_\infty = \frac{\mu_\infty^* c_{p,\infty}^*}{\kappa_\infty^*}, \quad \mathrm{Sc}_\infty = \frac{\mu_\infty^*}{\rho_\infty^* D_\infty^*},
\end{aligned} \tag{3}$$

where a_f is the frozen speed of sound, and $\gamma_f = c_{p,\mathrm{tr}}/c_{v,\mathrm{tr}}$ the frozen specific heat ratio.

The ten basic variables in Eq. (2) are $\boldsymbol{q} = [\rho, u, v, w, T, Y_s, T_v]$, with $s \in [2, 5]$. Equation (2) can be expressed in an operator form as

$$\mathscr{N}(\boldsymbol{q}) = \mathbf{S}(\boldsymbol{q}), \tag{4}$$

where the operator $\mathscr{N}$ includes unsteady, convection and diffusion terms, and $\mathbf{S}$ represents the TCNE source term. The combination of ρ and four Y_s is chosen instead of five ρ_s because once Y_s and T_v are fixed as constants, Eq. (2) reduces to the same form as that for CPG flows $[\mathscr{N}(\boldsymbol{q}) = \mathbf{0}]$.

B. Mean flow solver

A laminar mean flow field is needed in advance to perform stability analyses. Here the mean flow is obtained by solving the parabolic boundary layer equation when viscous interactions are negligible. The Mangler-Levy-Lees transformation is introduced to obtain a rectangular computational domain [31]:

$$\begin{cases} d\xi = \rho_e U_e \mu_e r_0^{2j}\, dx \\ d\eta = \dfrac{U_e r^j \rho}{\sqrt{\xi}}\, dy \end{cases} \quad \text{where} \quad j = \begin{cases} 0 & \text{for two-dimensional flows} \\ 1 & \text{for axisymmetric flows} \end{cases}. \tag{5}$$

Here r is the radius. Due to the presence of TCNE source terms and transverse curvature (for cones), the boundary layer profile is not self-similar, so a streamwise marching procedure is employed [32]. Chebyshev collocation point method and the third-order finite-difference scheme are utilized, respectively, for discretization in the wall-normal and streamwise directions. The implicit Newtonian iteration is employed for local convergence. The wall boundary conditions adopted are no-slip, adiabatic or isothermal, and noncatalytic $[(\partial Y_s/\partial n)_w = 0]$ for all species.

C. Parabolized stability equations

The linear and nonlinear PSE solvers for TCNE flows were described and verified in the authors' previous works [7,33] and are thus briefly described below. The quantity $\boldsymbol{q}$ is decomposed into a steady laminar part $\bar{\boldsymbol{q}}$ and a perturbed part $\tilde{\boldsymbol{q}}$, where $\bar{\boldsymbol{q}} = [\bar{\rho}, \bar{U}, \bar{V}, \bar{W}, \bar{T}, \bar{Y}_s, \bar{T}_v]$ and $\tilde{\boldsymbol{q}} = [\tilde{\rho}, \tilde{u}, \tilde{v}, \tilde{w}, \tilde{T}, \tilde{y}_s, \tilde{T}_v]$. The governing equation for the disturbance is derived through

$$\mathscr{N}(\bar{\boldsymbol{q}} + \tilde{\boldsymbol{q}}) - \mathscr{N}(\bar{\boldsymbol{q}}) = \mathbf{S}(\bar{\boldsymbol{q}} + \tilde{\boldsymbol{q}}) - \mathbf{S}(\bar{\boldsymbol{q}}), \tag{6}$$

which can be expanded into a matrix form:

$$\begin{aligned}
&\boldsymbol{F}\frac{\partial \tilde{\boldsymbol{q}}}{\partial t} + \boldsymbol{A}\frac{\partial \tilde{\boldsymbol{q}}}{\partial x} + \boldsymbol{B}\frac{\partial \tilde{\boldsymbol{q}}}{\partial y} + \boldsymbol{C}\frac{\partial \tilde{\boldsymbol{q}}}{\partial z} + \boldsymbol{D}\tilde{\boldsymbol{q}} \\
&= \boldsymbol{H}_{xx}\frac{\partial^2 \tilde{\boldsymbol{q}}}{\partial x^2} + \boldsymbol{H}_{yy}\frac{\partial^2 \tilde{\boldsymbol{q}}}{\partial y^2} + \boldsymbol{H}_{zz}\frac{\partial^2 \tilde{\boldsymbol{q}}}{\partial z^2} + \boldsymbol{H}_{xy}\frac{\partial^2 \tilde{\boldsymbol{q}}}{\partial x \partial y} + \boldsymbol{H}_{yz}\frac{\partial^2 \tilde{\boldsymbol{q}}}{\partial y \partial z} + \boldsymbol{H}_{xz}\frac{\partial^2 \tilde{\boldsymbol{q}}}{\partial x \partial z} + \boldsymbol{N}.
\end{aligned} \tag{7}$$

Here the first 11 terms are the linear terms of $\widetilde{\boldsymbol{q}}$. $\boldsymbol{F}$, $\boldsymbol{A}$, $\boldsymbol{B}$, $\boldsymbol{C}$, $\boldsymbol{D}$, and $\boldsymbol{H}$ are all 10×10 matrices, only related to the mean flow $\bar{\boldsymbol{q}}$. $\boldsymbol{N}$ represents the nonlinear term, containing the square and higher-order terms of $\widetilde{\boldsymbol{q}}$. Different from that in incompressible flows where $\boldsymbol{N}_{\text{inc}} = -\widetilde{u} \cdot \nabla \widetilde{u}$, $\boldsymbol{N}$ here contains much more terms and is also related to $\bar{\boldsymbol{q}}$ as there are products of more than three variables in Eq. (2). The software MAPLE is utilized to ensure the correctness of these complex matrix expressions. The following Fourier decomposition is introduced for the disturbance and nonlinear term:

$$\begin{aligned}\widetilde{\boldsymbol{q}}(x, y, z, t) &= \sum_{m,n} \hat{\boldsymbol{q}}_{mn}(x, y) \exp\left[i\left(\int_{x_0}^{x} \alpha_{mn}(\bar{x}) d\bar{x} + n\beta z - m\omega t\right)\right],\\ \boldsymbol{N}(x, y, z, t) &= \sum_{m,n} \hat{\boldsymbol{N}}_{mn}(x, y) \exp\left[i(n\beta z - m\omega t)\right],\end{aligned} \tag{8}$$

where β and ω are the specified spanwise wave number and circular frequency, $\alpha_{mn} = \alpha_{r,mn} + i\alpha_{i,mn}$ the complex streamwise wave number, $\hat{\boldsymbol{q}}_{mn}$ the mode shape function. $\hat{\boldsymbol{N}}_{mn}$ contains all the possible nonlinear effects on mode (m, n) from other modes. Here the notation (m, n) denotes the mode with frequency of $m\omega$ and spanwise wave number and $n\beta$, respectively. As a result, the parabolized governing equation is written as

$$\hat{\mathbf{A}}_{mn} \frac{\partial \hat{\boldsymbol{q}}_{mn}}{\partial x} = -\hat{\mathbf{D}}_{mn} \hat{\boldsymbol{q}}_{mn} - \hat{\mathbf{B}}_{mn} \frac{\partial \hat{\boldsymbol{q}}_{mn}}{\partial y} - \hat{\mathbf{C}}_{mn} \frac{\partial^2 \hat{\boldsymbol{q}}_{mn}}{\partial y^2} + \hat{\boldsymbol{N}}_{mn} \exp\left(-i \int \alpha_{mn} dx\right), \tag{9}$$

which enables a procedure of streamwise marching. The rearranged matrices $\hat{\mathbf{A}}_{mn}$, $\hat{\mathbf{B}}_{mn}$, $\hat{\mathbf{C}}_{mn}$, and $\hat{\mathbf{D}}_{mn}$ are functions of α_{mn}, $m\omega$, $n\beta$, and the matrices in Eq. (7). $\hat{\boldsymbol{N}}_{mn}$ is the nonlinear forcing term. A phase speed is defined as $c_{r,mn} = m\omega/\alpha_{r,mn}$. The circular frequency ω is related to the disturbance frequency f^* through

$$\frac{\omega}{\text{Re}_L} = F = \frac{2\pi f^*}{\text{Re}_\infty U_\infty^*}, \tag{10}$$

where F is the global nondimensional frequency. The global spanwise wave number $B = \beta/\text{Re}_L$ is similarly defined. If $\hat{\boldsymbol{N}}_{mn}$ is ignored, the equation for each mode is decoupled from each other to give the linear PSE analyses. In LST, the nonparallel terms related to the streamwise derivatives are further neglected, leading to an eigenvalue problem. Note that in PSE the growth rate σ is not unique and depends on a specific quantity $\hat{\varphi}$:

$$\sigma_\varphi = -\alpha_i + \text{iRe}\left(\frac{1}{\hat{\varphi}} \frac{\partial \hat{\varphi}}{\partial x}\right). \tag{11}$$

In this paper, $\hat{\varphi}$ is selected to be the disturbance energy $\sqrt{\hat{E}}$ to be defined in Sec. II D.

The disturbance boundary conditions at the wall are

$$\hat{u} = \hat{v} = \hat{w} = \hat{T} = \hat{T}_v = \hat{y}_s = 0 \quad \text{at} \quad y = 0. \tag{12}$$

However, for steady modes $(m = 0)$, the wall-boundary conditions are the same as those of the laminar flow. In the far field, a nonreflective far-field boundary is employed [34]. The wall-normal discretization employs Chebyshev collocation point method, while the streamwise discretization employs a backward finite-difference scheme.

D. Energy norm and budget equations

With the solutions of Eq. (9) in hand, the energy transfer mechanisms can be further analyzed for modal disturbances. The energy norm $\widetilde{E}$ needs to include the contribution from every component of $\widetilde{\boldsymbol{q}}$:

$$2\widetilde{E} = \|\widetilde{\boldsymbol{q}}\|_E = \widetilde{\boldsymbol{q}}^{\text{H}} \boldsymbol{M} \widetilde{\boldsymbol{q}}, \tag{13}$$

where $\boldsymbol{M}$ is a symmetric positive-definite matrix. The energy norm of CPG, derived in Refs. [17,19], takes the form

$$\widetilde{\boldsymbol{q}}^{\mathrm{CPG}} = [\widetilde{\rho},\ \widetilde{u},\ \widetilde{v},\ \widetilde{w},\ \widetilde{T}]^{\mathrm{T}}, \quad \boldsymbol{M}^{\mathrm{CPG}} = \mathrm{diag}\left(\left[\frac{R\bar{T}}{\bar{\rho}},\ \bar{\rho},\ \bar{\rho},\ \bar{\rho},\ \frac{\bar{\rho}\bar{c}_v}{\mathrm{Ec}_\infty \bar{T}}\right]\right). \tag{14}$$

As a result, the disturbance energy satisfies the following linearized equation on a uniform basic flow without external sources:

$$\begin{aligned}\frac{\partial \widetilde{E}^{\mathrm{CPG}}}{\partial t} &\equiv \frac{1}{2}\frac{\partial}{\partial t}\left(\bar{\rho}|\widetilde{\boldsymbol{u}}|^2 + \frac{R\bar{T}}{\bar{\rho}}\widetilde{\rho}^2 + \frac{\bar{\rho}\bar{c}_v}{\mathrm{Ec}_\infty \bar{T}}\widetilde{T}^2\right)\\ &= -\nabla\cdot(\widetilde{p}\widetilde{\boldsymbol{u}}) + \nabla\cdot(\widetilde{\boldsymbol{u}}\cdot\widetilde{\boldsymbol{\tau}}) + \nabla\cdot\left(\frac{\bar{\kappa}}{\mathrm{Ec}_\infty \bar{T}}\widetilde{T}\nabla\widetilde{T}\right) - \widetilde{\boldsymbol{\tau}} : \nabla\widetilde{\boldsymbol{u}} - \frac{\bar{\kappa}}{\mathrm{Ec}_\infty \bar{T}}\nabla\widetilde{T}\cdot\nabla\widetilde{T},\end{aligned} \tag{15}$$

where the coordinates are moving with fluids, and the disturbances of μ and κ are not considered. Equation (15) can be integrated over some space region Ω. As a result, the first three terms on the right-hand side is eliminated using Gauss theorem of divergence, if one of the following properties are satisfied [12]: (1) the disturbances are periodic in space and (2) the velocity and temperature disturbances tend to zero at the wall or in the far field. Consequently, the integration of Eq. (15) is written as

$$\frac{\partial}{\partial t}\int_\Omega \widetilde{E}^{\mathrm{CPG}}\, d\Omega = -\int_\Omega \widetilde{\boldsymbol{\tau}} : \nabla\widetilde{\boldsymbol{u}}\, d\Omega - \int_\Omega \frac{\bar{\kappa}}{\mathrm{Ec}_\infty \bar{T}}\nabla\widetilde{T}\cdot\nabla\widetilde{T}\, d\Omega \leqslant 0, \tag{16}$$

which shows that the energy defined in Eq. (14) for CPG is monotonically nonincreasing in time in the absence of energy/force sources and other external energy inputs.

The physical meaning of $\widetilde{E}^{\mathrm{CPG}}$ is seen more easily in terms of the disturbance pressure $\widetilde{p}$ and entropy $\widetilde{s}$, instead of $\widetilde{\rho}$ and $\widetilde{T}$:

$$\widetilde{E}^{\mathrm{CPG}} = \frac{1}{2}\left[\bar{\rho}|\widetilde{\boldsymbol{u}}|^2 + \bar{\rho}\bar{a}^2\left(\frac{\widetilde{p}}{\gamma\bar{p}}\right)^2 + \frac{\gamma-1}{\gamma}\bar{p}\left(\frac{\widetilde{s}}{\mathrm{Ec}_\infty R}\right)^2\right], \tag{17}$$

where a is the speed of sound. The first two terms on the right-hand side are recognized as the total energy of sound waves ($\widetilde{s}=0$) in acoustics, with the second term resulting from the pressure work through compression and expansion. The third term represents the energy from heat exchange. It is known that a disturbance on a uniform basic flow can be decomposed into a vorticity component (transverse velocities only), an entropy component (isobaric), as well as fast and slow acoustic components (isentropic). George and Sujith [18] showed that in the form of Eq. (14), the eigenvectors of these components were orthogonal to each other, making the system self-adjoint.

For TCNE flows, the same procedure as that for CPG is implemented to derive the expression of the energy norm. The disturbance equations [see Eq. (7)] on a uniform basic flow are combined together so that the pressure-related terms appear only in the form of $\nabla\cdot(\widetilde{p}\widetilde{\boldsymbol{u}})$. The combined equation is written as

$$\begin{aligned}&\frac{1}{2}\frac{\partial}{\partial t}\left(\bar{\rho}|\widetilde{\boldsymbol{u}}|^2 + \sum_s \frac{\bar{T}R_s}{\bar{\rho}_s}\widetilde{\rho}_s^2 + \frac{\bar{\rho}\bar{c}_{v,\mathrm{tr}}}{\mathrm{Ec}_\infty \bar{T}}\widetilde{T}^2 + \frac{\bar{\rho}\bar{c}_{vib}}{\mathrm{Ec}_\infty \bar{T}}\widetilde{T}_v^2\right)\\ &\quad = -\nabla\cdot(\widetilde{p}\widetilde{\boldsymbol{u}}) + \left(\frac{\bar{T}R_s}{\bar{\rho}_s}\widetilde{\rho}_s - \frac{\bar{e}_s}{\mathrm{Ec}_\infty \bar{T}}\widetilde{T}\right)\widetilde{\omega}_s + \frac{\widetilde{Q}_{t-v}}{\mathrm{Ec}_\infty \bar{T}}(\widetilde{T}_v - \widetilde{T}) + \mathrm{vis.},\end{aligned} \tag{18}$$

where vis. represents the complicated viscous terms. After a spatial integration, the pressure-work term $\nabla\cdot(\widetilde{p}\widetilde{\boldsymbol{u}})$ is eliminated, while the second and third terms on the right-hand side are the energy exchange by the TCNE source terms. The resulting form of the energy norm for TCNE flows is written as

$$2\widetilde{E} = \underbrace{\bar{\rho}|\widetilde{\boldsymbol{u}}|^2}_{\mathrm{EU}} + \underbrace{\frac{\bar{T}R}{\bar{\rho}}\widetilde{\rho}^2 + \bar{\rho}\bar{T}\widetilde{\boldsymbol{Y}}^{\mathrm{H}}\boldsymbol{R}_Y\widetilde{\boldsymbol{Y}} + 2\bar{T}\sum_m (R_m - R_1)\widetilde{\rho}\widetilde{Y}_m}_{\mathrm{ED}} + \underbrace{\frac{\bar{\rho}\bar{c}_{v,\mathrm{tr}}}{\mathrm{Ec}_\infty \bar{T}}\widetilde{T}^2 + \frac{\bar{\rho}\bar{c}_{vib}}{\mathrm{Ec}_\infty \bar{T}}\widetilde{T}_v^2}_{\mathrm{ET}} = \widetilde{\boldsymbol{q}}^{\mathrm{H}}\boldsymbol{M}\widetilde{\boldsymbol{q}}, \tag{19}$$

where the notations of EU, ED, and ET are introduced for later discussion in Sec. III. Here $\widetilde{\rho}_s$ has been replaced with $\widetilde{\rho}$ and $\widetilde{Y}_s$, and the expressions of the matrices are

$$\boldsymbol{R}_Y = R_1\begin{bmatrix} 1111 \\ 1111 \\ 1111 \\ 1111 \end{bmatrix} + \begin{bmatrix} R_2 & & & \\ & R_3 & & \\ & & R_4 & \\ & & & R_5 \end{bmatrix} \quad \widetilde{\boldsymbol{Y}} = \begin{bmatrix} Y_2 \\ Y_3 \\ Y_4 \\ Y_5 \end{bmatrix}, \tag{20}$$

$$\boldsymbol{M} = \begin{bmatrix} \frac{\bar{T}R}{\bar{\rho}} & & & & & (R_m - R_1)\bar{T} & \\ & \bar{\rho} & & & & & \\ & & \bar{\rho} & & & & \\ & & & \bar{\rho} & & & \\ & & & & \frac{\bar{\rho}\bar{c}_{v,\mathrm{tr}}}{\mathrm{Ec}_\infty \bar{T}} & & \\ (R_s - R_1)\bar{T} & & & & & \bar{\rho}\bar{T}R_{Y,sm} & \\ & & & & & & \frac{\bar{\rho}\bar{c}_{vib}}{\mathrm{Ec}_\infty \bar{T}} \end{bmatrix} \quad s, m \in [2, 5]. \tag{21}$$

Although $\boldsymbol{M}$ is not diagonal, it is positive definite, meeting the requirement of energy-norm definition.

The governing equation of the disturbance energy in boundary layer flows are obtained through left-multiplying $\widetilde{\boldsymbol{q}}^{\mathrm{H}}\boldsymbol{M}\boldsymbol{F}^{-1}$ to Eq. (7). As the terms in the equation are numerous, they are classified on their physical properties. Matrix $\boldsymbol{A}$ (also $\boldsymbol{B}$ and $\boldsymbol{C}$) contains the terms related to convection, pressure work, and viscous transport:

$$\boldsymbol{A} = \bar{U}\boldsymbol{F} + \boldsymbol{A}^{\text{p-s}} + \boldsymbol{A}^{\text{vis}}. \tag{22}$$

The elements in $\boldsymbol{D}$ are from the pressure-work, production, viscous transportation, and TCNE source terms, respectively:

$$\boldsymbol{D} = \boldsymbol{D}^{\text{p-s}} + \boldsymbol{D}^{\text{prod}} + \boldsymbol{D}^{\text{vis}} + \boldsymbol{D}^{\text{src}}, \quad \boldsymbol{D}^{\text{prod}} = \boldsymbol{D}^{\text{nrm}} + \boldsymbol{D}^{\text{npara}}. \tag{23}$$

Here $\boldsymbol{D}^{\text{prod}}$ is further divided into two parts: the first part $\boldsymbol{D}^{\text{nrm}}$ is related only to the wall-normal derivatives of basic flow ($\partial\bar{\boldsymbol{q}}/\partial y$); the second part $\boldsymbol{D}^{\text{npara}}$ comes from the nonparallelism of the boundary layer flow ($\partial\bar{\boldsymbol{q}}/\partial x$ and $\bar{V}$). The elements in $\boldsymbol{H}$ are all from the viscous transportation.

The classified governing equation is written as

$$\frac{D\widetilde{E}}{Dt} = \mathcal{L} + \mathcal{N}, \quad \mathcal{L} = \mathcal{P} + \Xi + \Pi + \mathcal{V} + \mathcal{S}, \tag{24}$$

where $\mathcal{L}$ and $\mathcal{N}$ represent the energy transfer through linear and nonlinear mechanisms, respectively. The specific expressions of these terms are the following:

(i) *Material derivative of the disturbance energy:*

$$\frac{D\widetilde{E}}{Dt} = \frac{\partial\widetilde{E}}{\partial t} + \bar{U}\frac{\partial\widetilde{E}}{\partial x} = \frac{\partial\widetilde{E}}{\partial t} + \bar{U}\widetilde{\boldsymbol{q}}^{\mathrm{H}}\boldsymbol{M}\frac{\partial\widetilde{\boldsymbol{q}}}{\partial x} + \frac{1}{2}\bar{U}\widetilde{\boldsymbol{q}}^{\mathrm{H}}\frac{\partial\boldsymbol{M}}{\partial x}\widetilde{\boldsymbol{q}} \tag{25a}$$

(ii) *Work done by the pressure disturbance:*

$$\Pi = -\frac{1}{2}\widetilde{\boldsymbol{q}}^{\mathrm{H}}\boldsymbol{MF}^{-1}\left(\boldsymbol{A}^{\text{p-s}}\frac{\partial\widetilde{\boldsymbol{q}}}{\partial x}+\boldsymbol{B}^{\text{p-s}}\frac{\partial\widetilde{\boldsymbol{q}}}{\partial y}+\boldsymbol{C}^{\text{p-s}}\frac{\partial\widetilde{\boldsymbol{q}}}{\partial z}+\boldsymbol{D}^{\text{p-s}}\widetilde{\boldsymbol{q}}\right)+\text{c.c.} = -\mathrm{Re}\,(\underbrace{\widetilde{\boldsymbol{u}}^{\dagger}\cdot\nabla\widetilde{p}}_{\mathrm{DF}}+\underbrace{\widetilde{p}^{\dagger}\nabla\cdot\widetilde{\boldsymbol{u}}}_{\mathrm{DL}}) \tag{25b}$$

where † and c.c. denote complex conjugate. DF and DL represent the energy transfer due to pressure diffusion and dilatation.

(iii) *Production term (wall-normal derivatives only):*

$$\mathcal{P} = -\frac{1}{2}\widetilde{\boldsymbol{q}}^{\mathrm{H}}\boldsymbol{MF}^{-1}\boldsymbol{D}^{\mathrm{nrm}}\widetilde{\boldsymbol{q}}+\text{c.c.} = -\mathrm{Re}\Bigg[\overbrace{\bar{\rho}\widetilde{u}^{\dagger}\widetilde{v}\frac{\partial\bar{U}}{\partial y}}^{\mathrm{PU}}+\overbrace{\frac{\bar{\rho}}{\mathrm{Ec}_{\infty}\bar{T}}\widetilde{v}\left(\bar{c}_{v,\mathrm{tr}}\widetilde{T}^{\dagger}\frac{\partial\bar{T}}{\partial y}+\bar{c}_{vib}\widetilde{T}_{v}^{\dagger}\frac{\partial\bar{T}_{v}}{\partial y}\right)}^{\mathrm{PT}}$$
$$+\underbrace{\left(\frac{R}{\bar{\rho}}\widetilde{\rho}^{\dagger}+(R_m-R_1)\widetilde{Y}_m^{\dagger}\right)\widetilde{v}\bar{T}\frac{\partial\bar{\rho}}{\partial y}+\left((R_m-R_1)\widetilde{\rho}^{\dagger}+\bar{\rho}R_{Y,sm}\widetilde{Y}_s^{\dagger}\right)\widetilde{v}\bar{T}\frac{\partial\bar{Y}_m}{\partial y}}_{\mathrm{PD}}\Bigg] \tag{25c}$$

The production term represents the energy transfer from the mean flow to the disturbance. Note that the first term of $\mathcal{P}$, PU, comes from the Reynolds stress. Besides, there is energy transfer due to the gradients of the temperature, density, and species mass fractions of the basic flow (PT and PD).

(iv) *Production term due to nonparallelism:*

$$\Xi = -\frac{1}{2}\widetilde{\boldsymbol{q}}^{\mathrm{H}}\left(\boldsymbol{MF}^{-1}\boldsymbol{D}^{\mathrm{npara}}\widetilde{\boldsymbol{q}}+\bar{V}\boldsymbol{M}\frac{\partial\widetilde{\boldsymbol{q}}}{\partial y}-\frac{1}{2}\bar{U}\frac{\partial\boldsymbol{M}}{\partial x}\widetilde{\boldsymbol{q}}\right)+\text{c.c.} \tag{25d}$$

(v) *Viscous diffusion and dissipation:*

$$\mathcal{V} = \frac{1}{2}\widetilde{\boldsymbol{q}}^{\mathrm{H}}\boldsymbol{MF}^{-1}\left(-\boldsymbol{A}^{\mathrm{vis}}\frac{\partial\widetilde{\boldsymbol{q}}}{\partial x}-\boldsymbol{B}^{\mathrm{vis}}\frac{\partial\widetilde{\boldsymbol{q}}}{\partial y}-\boldsymbol{C}^{\mathrm{vis}}\frac{\partial\widetilde{\boldsymbol{q}}}{\partial z}-\boldsymbol{D}^{\mathrm{vis}}\widetilde{\boldsymbol{q}}+\boldsymbol{H}_{xx}\frac{\partial^2\widetilde{\boldsymbol{q}}}{\partial x^2}\right.$$
$$\left.+\boldsymbol{H}_{xy}\frac{\partial^2\widetilde{\boldsymbol{q}}}{\partial x\partial y}+\boldsymbol{H}_{yy}\frac{\partial^2\widetilde{\boldsymbol{q}}}{\partial y^2}+\boldsymbol{H}_{xz}\frac{\partial^2\widetilde{\boldsymbol{q}}}{\partial x\partial z}+\boldsymbol{H}_{yz}\frac{\partial^2\widetilde{\boldsymbol{q}}}{\partial y\partial z}\right)+\text{c.c.} = \mathrm{VU}+\mathrm{VT}+\mathrm{VY}. \tag{25e}$$

The viscous term contains three parts: (1) VU, the terms related to velocity gradients; (2) VT, the terms related to the gradients of T and T_v; and (3) VY, the terms related to the gradients of Y_s. These three parts represent the diffusion and dissipation of momentum, energy, and mass, respectively.

(vi) *Energy transfer due to the disturbance of TCNE source terms:*

$$\mathcal{S} = -\tfrac{1}{2}\widetilde{\boldsymbol{q}}^{\mathrm{H}}\boldsymbol{MF}^{-1}\boldsymbol{D}^{\mathrm{src}}\widetilde{\boldsymbol{q}}+\text{c.c.} \tag{25f}$$

Here $\boldsymbol{D}^{\mathrm{src}}$ contains the derivatives of $\dot{\omega}_s$ and Q_{t-v} towards ρ, T, T_v, and Y_s.

(vii) *Energy transfer by nonlinear terms:*

$$\mathcal{N} = \tfrac{1}{2}\widetilde{\boldsymbol{q}}^{\mathrm{H}}\boldsymbol{MF}^{-1}N+\text{c.c.} \tag{25g}$$

Note that $\mathcal{L}$ represents the energy exchange between the mean flow and the disturbance, while $\mathcal{N}$ primarily represents the energy exchange among different Fourier modes of the disturbance. As it is related to $\bar{\boldsymbol{q}}$, $\mathcal{N}$ also contains the interactions among the mean flow and more than two modes.

To study the energy transfer of a single mode, $\widetilde{\boldsymbol{q}}$ is replaced with Eq. (8) for a single mode to give

$$\widetilde{E} = \frac{1}{2}\widehat{\boldsymbol{q}}^{\mathrm{H}}\boldsymbol{M}\widehat{\boldsymbol{q}}\exp\left(-2\int\alpha_i\,dx\right) \equiv \hat{E}\exp\left(-2\int\alpha_i\,dx\right). \tag{26}$$

Here the subscripts m and n are omitted for clarity. The other terms in Eq. (24) are transformed similarly. Special care is posed on the material derivative term, which is rewritten as

$$\frac{D\widetilde{E}}{Dt} = \bar{U}\left(\frac{\partial\hat{E}}{\partial x}-2\alpha_i\hat{E}\right)\exp\left(-2\int\alpha_i dx\right) = 2\sigma_E\bar{U}\hat{E}\exp\left(-2\int\alpha_i dx\right), \tag{27}$$

TABLE I. Free-stream parameters for the Mach 10 TCNE flow over a flat plate.

Ma_∞	Re_∞ (/m)	T^*_∞ (K)	p^*_∞ (Pa)	U^*_∞ (m/s)	$Y_{\mathrm{N}_2,\infty}$	T^*_w (K)
10	6.6×10^6	350	3582	3750	0.78	Adiabatic

where σ_E is the growth rate based on $\sqrt{\hat{E}}$. [see Eq. (11)]. Take $\sigma_E = \sigma_E(x)$ and integrate Eq. (27) along the wall-normal direction, which gives

$$\int_0^\infty \frac{D\widetilde{E}}{Dt}\, dy = 2\sigma_E \exp\left(-2\int \alpha_i dx\right)\int_0^\infty \bar{U}\hat{E}\, dy \equiv \sigma_E \Gamma. \tag{28}$$

Therefore, if the wall-normal integration is also made on the right-hand side of Eq. (24), then the direct contribution from each term is obtained to the growth rate. For example, the contribution from the linear mechanism $\mathcal{L}$ is

$$\sigma_{\mathcal{L}} = \int_0^\infty \mathcal{L}_\Gamma\, dy, \quad \mathcal{L}_\Gamma = \frac{\mathcal{L}}{\Gamma}, \tag{29}$$

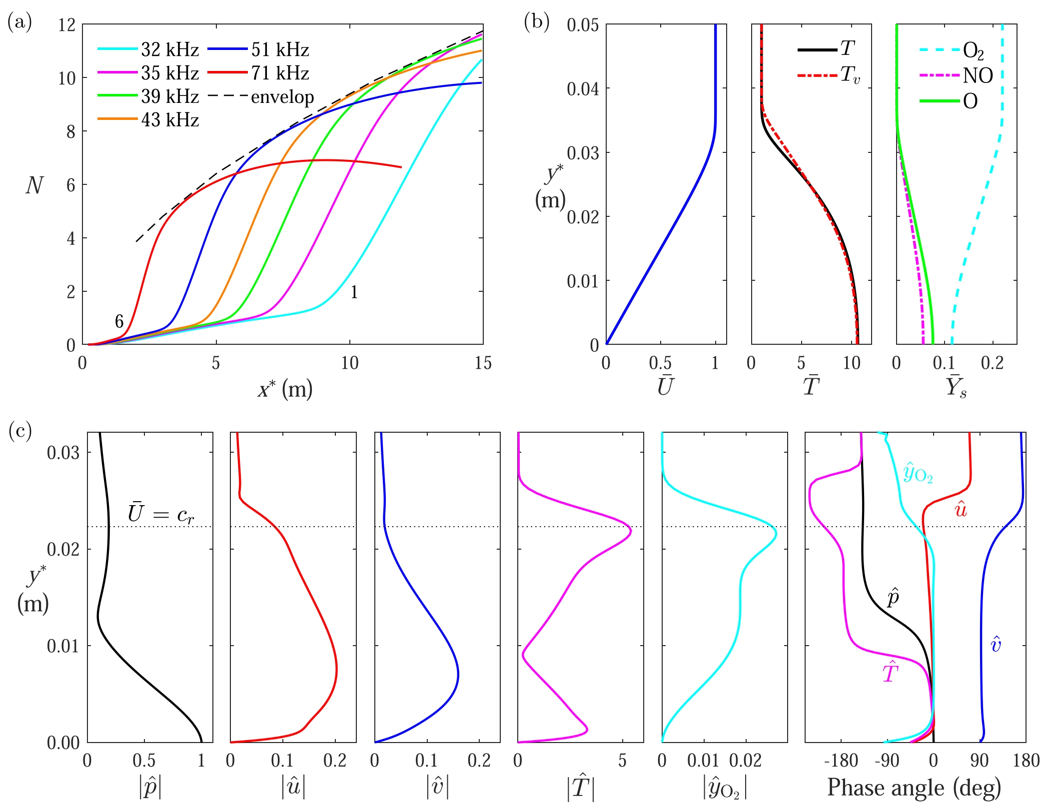

FIG. 1. Overall view of the LST results for the Mach 10 flat-plate flow: (a) N factor curves of two-dimensional waves, (b) mean flow profiles where the envelop of N reaches 10, and (c) shape functions of the second-mode disturbance with $f^* = 43\,\mathrm{kHz}$.

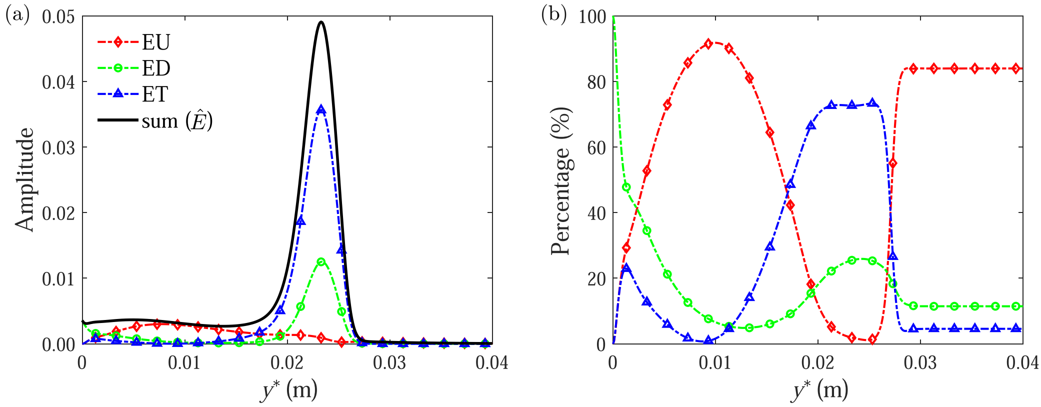

FIG. 2. Energy norm of the second-mode disturbance corresponding to the disturbance in Fig. 1(c): (a) energy amplitude, (b) ratio in amplitude of each component.

where $\mathcal{L}_\Gamma$ is defined as the contribution density of $\mathcal{L}$ to the growth rate. Consequently, the growth rate of the disturbance energy σ_E is divided into several parts based on Eq. (25):

$$\sigma_E = \sigma_\mathcal{L} + \sigma_\mathcal{N}, \quad \sigma_\mathcal{L} = \sigma_\mathcal{P} + \sigma_\Xi + \sigma_\Pi + \sigma_\mathcal{V} + \sigma_\mathcal{S}. \tag{30}$$

The similarly defined growth-rate decomposition was also applied in Refs. [20,22] for the instability analyses in CPG flows.

III. BENCHMARK CASE RESULTS

First, the basic characteristics of the disturbance energy transfer in the TCNE boundary layers are analyzed from linear instability results. The test case is a hypersonic and high-enthalpy flow over a flat plate, with the parameters, as listed in Table I, adopted from the classic reference by Malik and Anderson [5] using equilibrium-gas models and also Hudson *et al.* [35] using TCNE models.

An overall view of the LST results is provided in Fig. 1. The two-dimensional ($\beta = 0$) second mode has the largest growth rate and is thus responsible for the N factor curves in Fig. 1(a). The envelope of N reaches 10 at $x^* = 11.5$ m, which is evaluated as the transition onset in this case, and the corresponding disturbance frequency is 43 kHz. The laminar boundary-layer profiles at $x^* = 11.5$ m are plotted in Fig. 1(b). The vibrational temperature T_v is nearly identical to T as an indication of local thermal equilibrium. Around half of the oxygen is dissociated near the wall. Figure 1(c) plots the shape functions of the second mode with the frequency f^* of 43 kHz at $x^* = 6.1$ m where the growth rate is the highest. All the variables are normalized using the pressure disturbance at the wall. The velocity component $\hat{v}$ has comparative amplitude with $|\hat{u}|$, and their amplitude peaks are both located near the wall. In comparison, $|\hat{T}|$ and $|\hat{Y}_s|$ have peaks around the critical layer (where $\bar{U} = c_r$). At $y^* < 8$ mm, the phase angles of all the variables are near 0 except for $\hat{v}$, whose phase is around 90° larger. The phase difference is key to the energy transfer process, as discussed later.

As defined in Eq. (19), the energy norm of the second-mode disturbance related to Fig. 1(c) is plotted in Fig. 2. Different from the shape functions, the peak value of $\hat{E}$ around the critical layer is over 12 times larger than those in the near-wall region. This peak is formed owing to the large amplitudes of ET and ED there. Figure 2(b) gives the contribution from each component by percentage. It is seen that over half of $\hat{E}$ comes from the kinetic energy (EU) at 3 mm $< y^* <$ 16 mm and $y^* >$ 29 mm, though the amplitude is relatively low.

The profiles of different terms in Eq. (24) are shown in Fig. 3 for the second-mode disturbance. In the LST calculation, the flow is assumed to be locally parallel, so $\Xi = 0$. The component of $\mathcal{P}$ [see

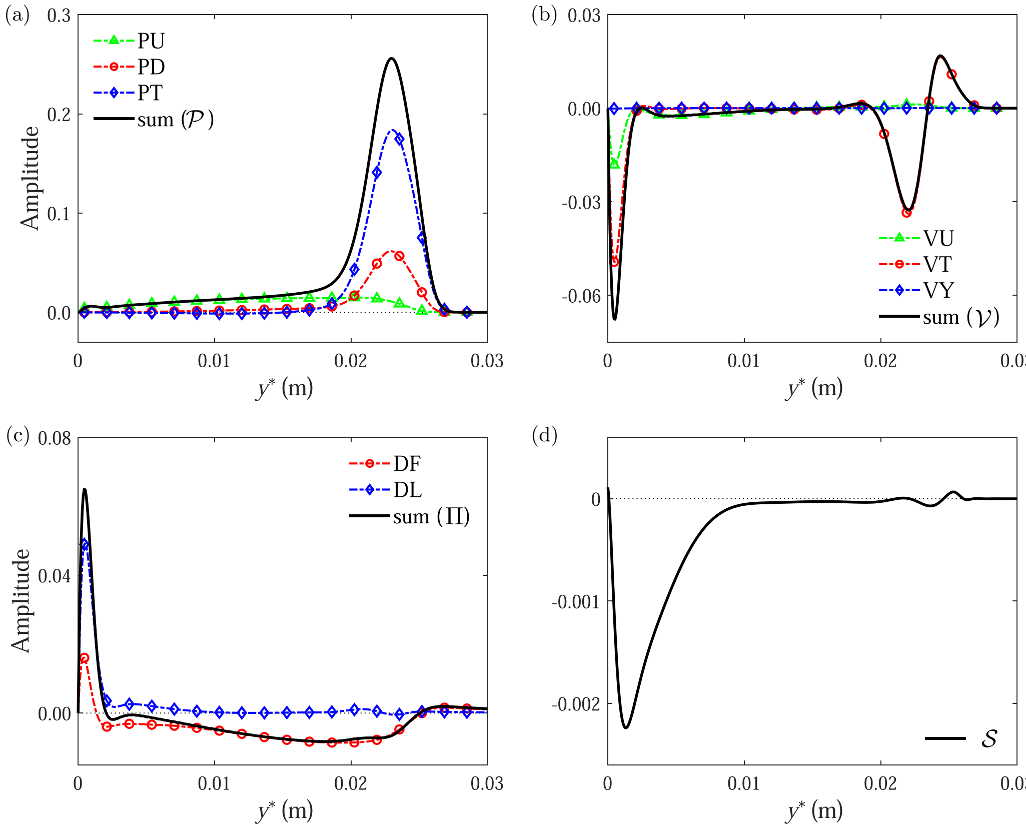

FIG. 3. Amplitude of different terms in the energy budget equation for the second mode: (a) production term $\mathcal{P}$, (b) viscous term $\mathcal{V}$, (c) pressure work term Π, and (d) TCNE source term $\mathcal{S}$.

Eq. (25c)] takes the form of $\mathrm{Re}(\bar{C}\hat{\varphi}^\dagger\hat{v})$, where $\bar{C}$ is a mean flow coefficient. Therefore, the sign of $\mathcal{P}$ is directly related to the phase difference between $\hat{v}$ and $\hat{\varphi}$. If the phase difference is exactly $\pm 90^\circ$, then $\mathrm{Re}(\hat{\varphi}^\dagger\hat{v}) = 0$. Consequently, $\mathcal{P}$ is relatively small at $y^* < 8$ mm. Only one peak is located near the critical layer in PT and PD, as also noted in Ref. [36]. In comparison, PU is mildly distributed throughout the boundary layer and makes most of the contribution to $\mathcal{P}$ at $y^* < 0.02$ m. For the viscous term $\mathcal{V}$, the contribution from the mass diffusion and dissipation (VY) is negligible. $\mathcal{V}$ acts as an energy sink in most regions with the largest contribution from VT. VU mainly contributes near the wall where the velocity gradients are large. VT also has a large amplitude close to the wall, despite the adiabatic boundary condition. This local extreme is owing to $\kappa_{\mathrm{tr}}\partial^2\hat{T}/\partial y^2$. It is observed that Π transfers the energy from the middle region of the boundary layer towards the wall. The pressure diffusion process (DF) consumes energy in most regions, while the pressure dilatation process (DL) positively contributes to the energy growth in the near-wall region. This positive contribution comes from the pressure work through fluid compression, and is associated with the acoustic nature of the second mode between the wall and the sonic line [37]. Besides, this dilatational pressure work can have considerable influence on the surface heat flux in the transitional region [38]. The TCNE source term $\mathcal{S}$ acts as an energy sink. This is consistent with the findings by [11,39] that the disturbances of TCNE source terms (endothermic reactions here) are stabilizing. Nevertheless, $\mathcal{S}$ is an order of magnitude smaller than the other terms in this case, which indicates that the effect of $\mathcal{S}$ on the energy growth is negligible. The same conclusion was drawn in [12] through an analysis on the disturbance

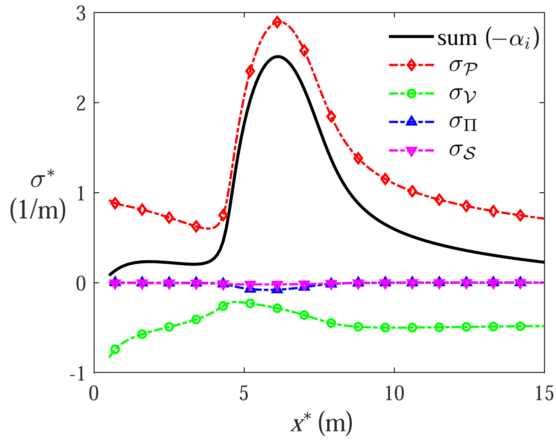

FIG. 4. Decomposition of the disturbance growth rate for the two-dimensional waves with $f^* = 43$ kHz.

Damköthler number. The present calculation provides more quantitative evidence from the energy's perspective.

Next, the contribution of each physical process to the disturbance growth rate is quantified using Eq. (30), as shown in Fig. 4. The disturbance gains energy from the mean flow through the production term $\mathcal{P}$ to support the growth of the first and second modes. On the other hand, the disturbance is stabilized by the viscous term $\mathcal{V}$ throughout the computational domain. This stabilization effect is the strongest in the most upstream location and continuously weakens downstream until $x^* = 4.8$ m. $|\sigma_{\mathcal{V}}|$ then begins to increase and remains nearly constant downstream of the second-mode region. It is widely known that the second-mode instability has an inviscid nature, where the inviscid production term $\mathcal{P}$ reaches its maximum. Furthermore, the results here show that the stabilizing effect of the viscous term is also minimal in the second-mode region, which reinforces the dominance of the second-mode instability. The overall contribution from the pressure work is offset through the integration in the wall-normal direction [see Eq. (18)], so $\sigma_{\Pi} \approx 0$ in most of the streamwise regions. It has a slightly stabilizing effect on the second mode, where the disturbance amplitude undergoes rapid amplification. $\sigma_{\mathcal{S}}$ is an order of magnitude smaller than the other terms.

Referring to Eq. (29), $\sigma_{\mathcal{P}}$ is the wall-normal integration of the contribution density $\mathcal{P}_{\Gamma}$. The contours of $\mathcal{P}_{\Gamma}$ and the other terms are displayed in Fig. 5. Here the y coordinate is normalized using the local nominal thickness δ, where $\bar{U}(\delta) = 0.99$, for clarity because the boundary layer thickness increases with x. As discussed in Fig. 3, the production term concentrates around the critical layer. This is consistent with the observation by Franko [36]. There is a region with negative $\mathcal{P}_{\Gamma}$ at $x^* < 2$ m because of negative PT and PD. This means that the energy is transferred back to the mean flow, whereas $\sigma_{\mathcal{P}}$ is still positive (see Fig. 4). On the contrary, $\mathcal{V}_{\Gamma}$ has a small concentration of positive values at $x^* < 2$ m, owing to the thermal diffusion, as shown in Fig. 5(b). Around the second-mode region, $|\mathcal{V}_{\Gamma}|$ decreases sharply near the critical layer, and its local peak in the wall-normal direction shifts to the near-wall region. The role of Π_{Γ} is to transfer the energy from the middle of the boundary layer towards the wall in the second-mode region. In the first-mode region, Π_{Γ} concentrates mainly around the boundary-layer edge. $\mathcal{S}_{\Gamma}$ primarily consumes the disturbance energy near the wall. The most affected region by $\mathcal{S}_{\Gamma}$ is the second-mode region. At last, the contours of $\mathcal{L}_{\Gamma}$, the sum of the above four terms, are plotted in Fig. 5(e). It is observed that Π_{Γ} and $\mathcal{V}_{\Gamma}$ are almost offset in the near-wall region, indicating an equilibrium between the diffusion and dissipation there. As a result, $\mathcal{L}_{\Gamma}$ distributes only near the critical layer, where the disturbance energy gains the largest growth.

The nonparallelism of the boundary layer flow, as neglected in LST, is investigated below by using linear PSE. As shown in Fig. 6(a), due to nonparallelism, σ_{Ξ} has a small positive contribution

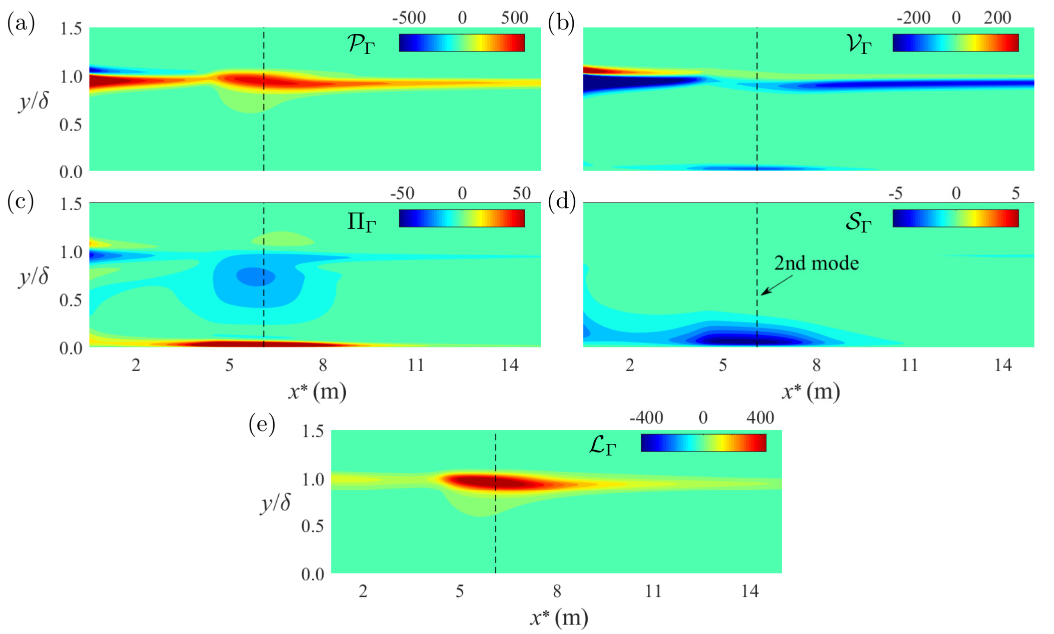

FIG. 5. Contours of the contribution density [see Eq. (29)] to the growth rate in the x-y plane: (a) production term $\mathcal{P}_\Gamma$, (b) viscous term $\mathcal{V}_\Gamma$, (c) pressure work term Π_Γ, (d) TCNE source term $\mathcal{S}_\Gamma$, and (e) sum of the former four $\mathcal{L}_\Gamma$.

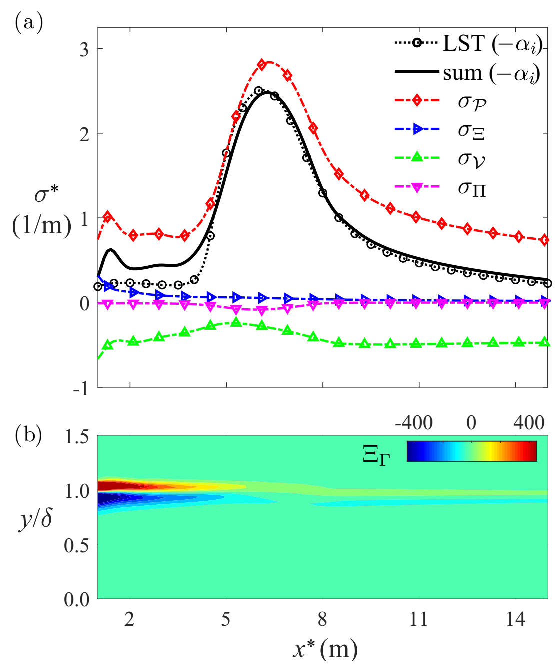

FIG. 6. Disturbance evolution from PSE: (a) decomposed growth rate and (b) contribution density contours of the nonparallelism term Ξ.

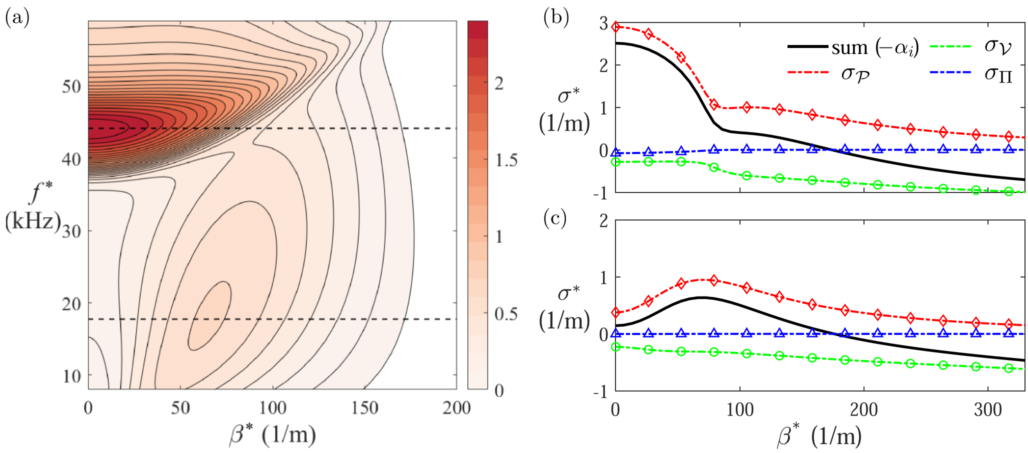

FIG. 7. Growth rate contours ($-\alpha_i^*$, 1/m) with different frequencies and spanwise wave numbers (a) as well as the growth-rate decomposition at the frequencies corresponding to the most unstable second (b) and first modes (c).

to the growth rate at $x^* < 4$ m, which is consistent with the previous finding that nonparallelism was slightly destabilizing and had more influence on the first mode [40]. Further downstream, σ_Ξ tends to zero and thus the growth rate from PSE is quite close to that from LST. The spatial distribution of Ξ_Γ is depicted in Fig. 6(b). The peaks and valleys in the wall-normal direction are all located near the critical layer. The maximum value of $|\Xi_\Gamma|$ in the first-mode region is even larger than $|\mathcal{P}_\Gamma|$, but the local net contribution σ_Ξ is small with the consideration of a wall-normal integration. Again, the analysis of the energy budget provides a way to quantitatively evaluate the effects of nonparallelism and to find out its spatial distribution.

The above discussions are limited to two-dimensional disturbances. It is known that the most unstable second mode is two-dimensional, while the most amplified first mode is three-dimensional, as presented in the growth rate contours in Fig. 7(a) at $x^* = 6.1$ m. The frequencies of the most unstable first and second modes are 18 kHz and 44 kHz, respectively. The growth-rate decompositions are calculated at these two frequencies for the most unstable first and second modes, to study the contributions of different terms for three-dimensional disturbances. For both modes, the stabilizing effect of $\mathcal{V}$ strengthens with the increase of β. In comparison, $\sigma_{\mathcal{P}}$ peaks at β^* of 73 /m in the first-mode case, causing the most unstable wave three-dimensional.

IV. CASES WITH DIFFERENT MEAN FLOW PARAMETERS

In this section, a parametric study is performed in terms of gas models, wall temperature T_w, free-stream Mach number Ma_∞ and free-stream temperature T_∞.

First, the benchmark case is recalculated using the CPG assumption for comparison. The same air composition and transport models (instead of Sutherland's law) as those in the TCNE case are employed for consistency. The comparisons of the mean flow profiles and two-dimensional disturbance growth rate by LST are plotted in Fig. 8 at x^* of 6.1 m. Due to the energy relaxation and chemical reactions, the wall-temperature for the TCNE case is 2140 K lower, so the density in the boundary layer rises and thus the nominal thickness decreases by 21%, compared to that in the CPG case. Consequently, the second mode is destabilized at a higher frequency in the TCNE case, as shown in Fig. 8. The growth rate decomposition is performed to identify the term responsible for this discrepancy. Figure 9 provides the distribution of $\sigma_{\mathcal{P}}$ and $\sigma_{\mathcal{V}}$ of the disturbance in the TCNE and CPG cases at x^* of 6.1 m. The contribution from σ_Π and $\sigma_{\mathcal{S}}$ is negligible and thus not shown. As can be seen, the two curves of $\sigma_{\mathcal{V}}$ are close to each other within the frequency range,

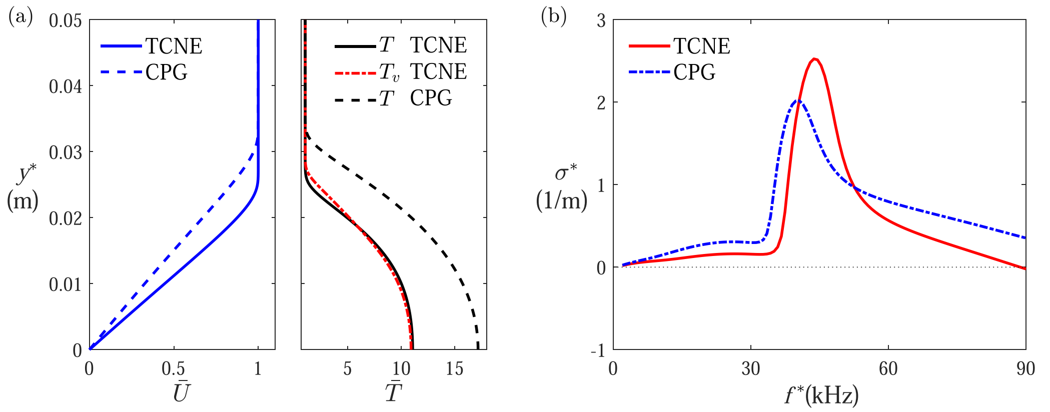

FIG. 8. (a) Mean flow profiles and (b) disturbance growth rate with different frequencies at x^* of 6.1 m for the Mach 10 flat-plate flow case in the TCNE and CPG flows.

though the difference tends to be slightly larger with frequency increase. The main difference in the second-mode growth rate comes from $\sigma_{\mathcal{P}}$. Again, it is concluded that compared with the CPG flow, TCNE changes the disturbance characteristics mainly through the mean flow modification.

Afterward, T_w in Table I is reduced to 1050 K to study the effects of wall cooling in the TCNE flow. As compared with that in Fig. 1, the location where the envelope of N reaches 10, moves upstream to $x^* = 7.9$ m at the disturbance frequency of 59 kHz. The laminar profiles at $x^* = 7.9$ m are depicted in Fig. 10(a). The maximum temperature in the boundary layer is less than 2000 K, which inhibits the excitation of vibrational energy and chemical dissociations. As a result, the thermal process is in nonequilibrium, and the species fractions remain almost chemically frozen. Figure 10(b) gives the streamwise distribution of the decomposed growth rates [see Eq. (30)]. Due to wall cooling, the first mode is suppressed to be stable, while the second mode is destabilized. The comparison with that in Fig. 4 shows that $\sigma_{\mathcal{P}}$ is more affected by wall cooling than $\sigma_{\mathcal{V}}$, mainly responsible for the stabilizing and destabilizing effects on modes. $\sigma_{\mathcal{V}}$ has similar streamwise distribution as that in the adiabatic-wall case and also reaches its maximum (minimum in absolute value) in the second-mode region.

The contribution densities of different terms are depicted in Fig. 11. The production term still concentrates near the critical layer though the mean flow gradients of temperature are large near the

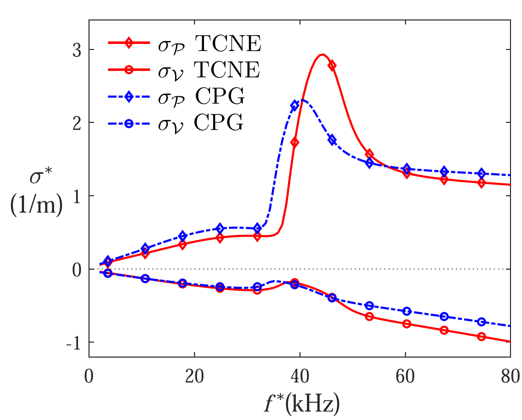

FIG. 9. Decomposition of the disturbance growth rate in the TCNE and CPG cases at x^* of 6.1 m.

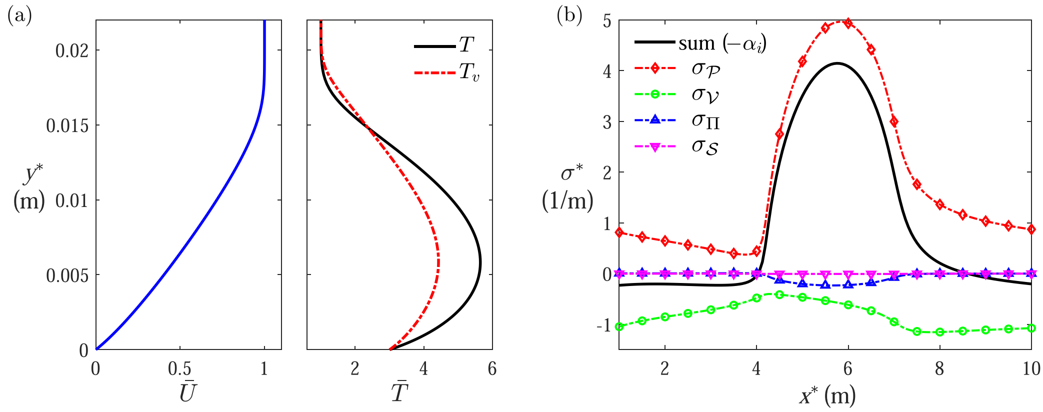

FIG. 10. (a) Mean flow profiles at N envelope of 10 and (b) distribution of the decomposed growth rate for the Mach 10 flat-plate flow case with cold wall.

wall with the isothermal boundary condition. There appears a positive region within $0.2 < y/\delta < 0.6$ around the second-mode region, as compared with that in Fig. 5. This contribution comes from the term PU. The distribution patterns of $\mathcal{V}_\Gamma$, Π_Γ, and $\mathcal{S}_\Gamma$ are all similar to those in the adiabatic-wall case. Again, Π_Γ and $\mathcal{V}_\Gamma$ almost offsets in the near wall region for the second mode. These are some universal characteristics of energy transfer mechanisms in terms of T_w variation.

Two more cases with Ma_∞ of 5 and 15 are investigated. The free-stream parameters T^*_∞, p^*_∞, and U^*_∞ remain the same, and both temperature boundary conditions are adiabatic. Figure 12 provides the laminar flow profiles at N of 10 ($x^* = 13.8$ m and 26.8 m for the two cases), as well as the decomposed disturbance growth rates at the corresponding frequencies ($f^* = 33$ kHz and 28 kHz). At Ma_∞ of 5, the temperature in the boundary layer is too low to trigger any chemical reactions. The vibrational energy is excited, and the difference in T^* and T^*_v at the wall is only 90 K. In the first-mode region ($x^* < 1$ m), both $\sigma_{\mathcal{P}}$ and $\sigma_{\mathcal{V}}$ have large amplitudes. Further downstream, $|\sigma_{\mathcal{V}}|$ continuously decreases and reaches its minimum in the second-mode region. In contrast, $\sigma_{\mathcal{P}}$ reaches its maximum there to allow a strong growth of disturbance. It is observed that $\sigma_{\mathcal{P}}$ has large values both in the first- and second-mode regions. It is the different amplitude of $\sigma_{\mathcal{V}}$ that leads to the significant difference in the growth rates between the first and second modes. Besides, σ_{Π} has a damping effect in the second-mode region and reduces $(-\alpha_i)$ by 15% at most. As shown in Fig. 12(c), when Ma_∞ reaches to 15, both T^* and T^*_v are over 5000 K, and thus the oxygen

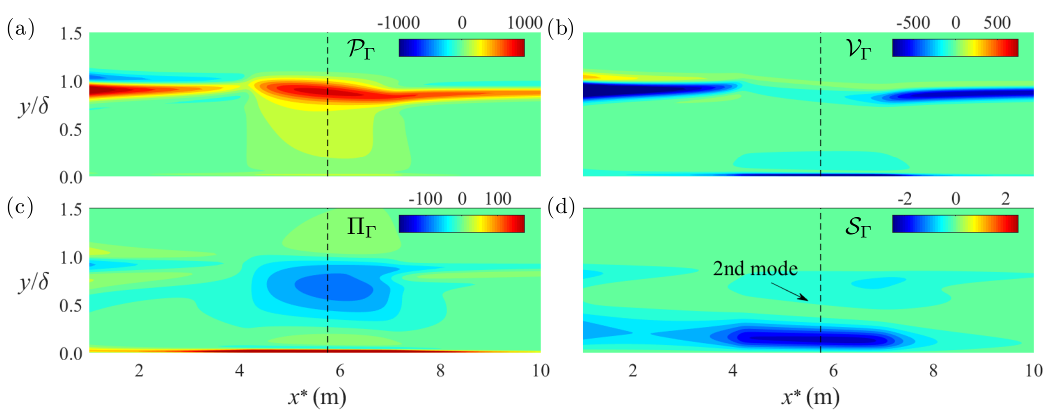

FIG. 11. Contours of the contribution density to the growth rate in the x-y plane with cold wall: (a) production term $\mathcal{P}_\Gamma$, (b) viscous term $\mathcal{V}_\Gamma$, (c) pressure work term Π_Γ, and (d) TCNE source term $\mathcal{S}_\Gamma$.

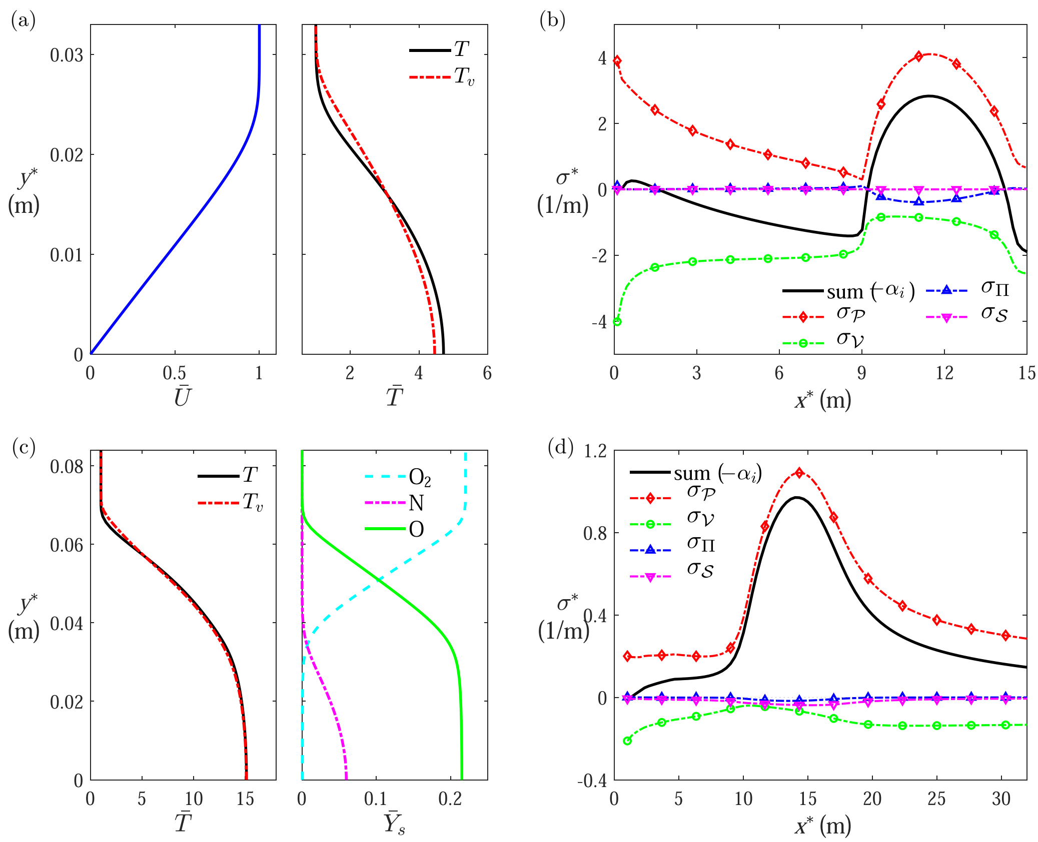

FIG. 12. Mean flow profiles at N envelope of 10 (a), (c) and the distribution of the decomposed growth rate (b, d) for the Mach 5 (a), (b) and Mach 15 (c), (d) flat-plate flow cases.

is almost dissociated within the boundary layer. At such a high Mach number, the second-mode growth is reduced due to strong compressibility [37], so it takes quite a long distance for the N factor envelope to reach 10. Although the vibrational energy and the monatomic species are highly excited, the contribution from $\sigma_{\mathcal{S}}$ is still small. It has a stabilizing effect of up to 5% on the second-mode growth rate.

The free-stream temperature is changed in the Mach 10 adiabatic-wall case to study the effects of TCNE. Two more cases with T_∞^* of 600 K and 900 K are considered with $\mathrm{Re}_\infty = 6.6 \times 10^6$ /m. These high free-stream temperatures can be obtained for flows behind an oblique head shock or from a high-enthalpy reservoir [41]. The laminar temperature and species profiles at x^* of 10 m are compared in Fig. 13(a). Higher T_∞^* leads to severer high-temperature effects. The mass fraction of the nitrogen atom exceeds 10% near the wall for the case with T_∞^* of 900 K. The boundary layer becomes thinner and cooler (in terms of the nondimensional temperature) with the increase of T_∞^*. Consequently, the maximum growth rate of the second mode increases and the corresponding streamwise location moves downstream, as shown in Fig. 13(b). Here the frequency $F = 1.1 \times 10^{-5}$ is set for all three cases. The streamwise distribution of $\sigma_{\mathcal{S}}$ is also plotted for comparison. Due to the damping effects of $\mathcal{S}$, the second-mode growth rates are reduced by as much as 5% and 6% in the cases with T_∞^* of 600 K and 900 K, respectively. Nevertheless, $\sigma_{\mathcal{S}}$ is not yet the dominant component in the second-mode growth even with T_∞^* of 900 K. The contribution densities of $\mathcal{S}$ are depicted in Fig. 14 at two different T_∞^*. $\mathcal{S}_\Gamma$ contributes mainly near the wall in the second-mode region for both cases, whose patterns bear a strong resemblance to that in Fig. 5 and are thus insensitive to T_∞^*.

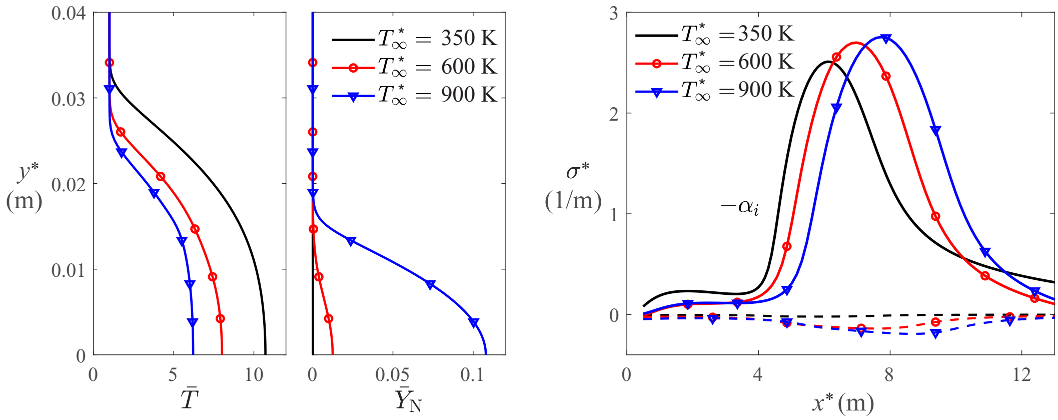

FIG. 13. Mean flow profiles at $x^* = 10$ m (a) and the distributions of decomposed growth rate (b) for the Mach 10 flat-plate flow cases with different T^*_∞.

V. NONLINEAR INSTABILITY RESULTS

The nonlinear process of the disturbance evolution is investigated in this section. An oblique-mode breakdown case is simulated here as one of the most important transition mechanisms in hypersonic boundary layers [42,43]. The Mach 10 flat-plate flow case with $T^*_\infty = 600$ K is adopted. The disturbance frequency F of the oblique mode (1, 1) is 1.1×10^{-5}, the same as that in Fig. 13, and the corresponding maximum N factor is around 10. The global spanwise wave number B of mode (1, 1) is selected to be 6×10^{-6} to cause large growth of the streamwise vortex mode (0, 2) and other modes. The initial disturbance amplitude of mode (1, 1), $A^0_{(1,1)}$, affects the relative strength of mode (0, 2), where the mode amplitudes are measured by the root mean square of the streamwise velocity disturbance $\widetilde{u}_{\mathrm{rms}}$. Here $A^0_{(1,1)}$ is set to 0.05% at the numerical inlet ($x^* = 4$ m) to simulate a natural transition condition. $A^0_{(1,1)}$ will be varied later to see its effects.

The streamwise amplitude development of the selected waves is displayed in Fig. 15(a). The evolution of mode (1, 1) from linear PSE is also plotted for reference. The amplitude discrepancy of mode (1, 1) between the linear and nonlinear calculations starts at x^* of 7.3 m with the amplitude of 0.07. The amplitude evolution of the two- and three-dimensional waves (2, 0) and (2, 2) is nearly identical throughout the domain. They are almost in saturation downstream x^* of 7.5 m. In contrast, the streamwise-vortex mode (0, 2) grows rapidly and exceeds (1, 1) in amplitude at x^* of 7.1 m, becoming dominant. Mode (0, 4) also experiences a dramatic amplification, as comparable to mode (0, 2) at $x^* = 8$ m.

The growth-rate decomposition in Eq. (30) is employed to distinguish the contribution from the linear and nonlinear mechanisms. The streamwise distribution of $\sigma_{\mathcal{L}}$ and $\sigma_{\mathcal{N}}$, along with their sum,

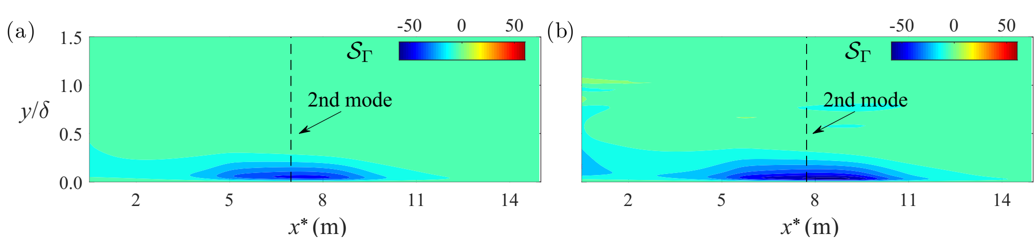

FIG. 14. Contribution density contours of the TCNE source term $\mathcal{S}_\Gamma$ to the growth rate in the x-y plane for the Mach 10 flat-plate flow cases with T^*_∞ of (a) 600 K and (b) 900 K.

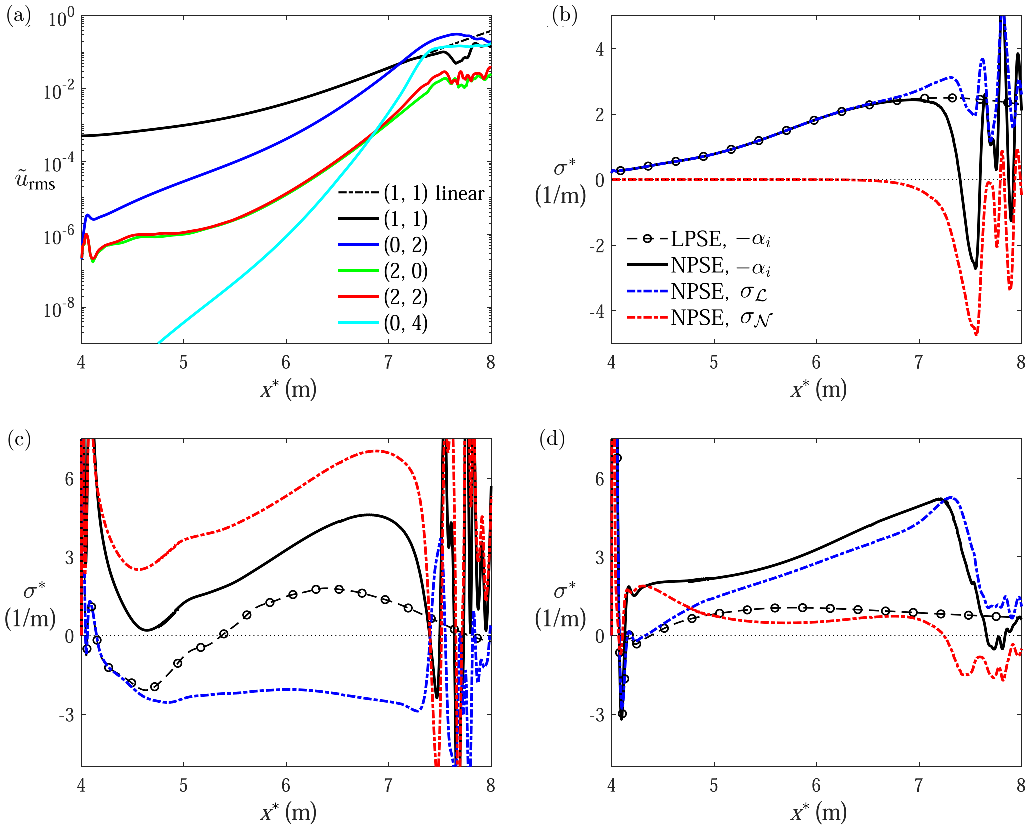

FIG. 15. Streamwise distributions of the disturbance modes' amplitudes (a) and decomposed growth rates [(b) for mode (1, 1), (c) for mode (2, 0), and (d) for mode (0, 2)] in the oblique breakdown case. The legends in (c) and (d) are the same as that in (b).

$-\alpha_i$, are all plotted in Figs. 15(b)–15(d) for modes (1, 1), (2, 0), and (0, 2), respectively. In the LPSE calculation, the nonlinear terms are neglected except at the inlet to initiate modes (2, 0) and (0, 2). For mode (1, 1), $\sigma_{\mathcal{L}}$ obtained from NPSE is even larger than that from LPSE downstream x^* of 6.5 m. However, $\mathcal{N}$ starts to strongly reduce the mode's growth when the harmonic waves attain relatively large amplitudes. This indicates that the oblique second mode obtains more energy from the mean flow and transfers it to the harmonic waves. Further downstream, strong oscillations are observed in the growth-rate curves. These oscillations were also observed in DNS calculations [44,45], which are mainly due to the highly inflectional flow profiles and complex nonlinear interactions when the harmonics are in large amplitudes. A further decomposition on $\sigma_{\mathcal{L}}$ shows that the oscillations are mainly caused by the production term, while the viscous term slightly changes. This shows that energy transfers rapidly back and forth among mode (1, 1), the mean flow, and other modes. Mode (2, 0) in the LPSE case first experiences damping upstream x^* of 5.3 m and then amplification. In comparison, $\sigma_{\mathcal{L}}$ of mode (2, 0) obtained from NPSE is lower than that from LPSE, and maintains at around -2.5 /m downstream x^* of 4.5 m. Thus, mode (2, 0) is more stable in terms of the basic flow due to the distortion by nonlinear interactions. However, mode (2, 0) from NPSE still has a relatively large growth rate ($-\alpha_i$) owing to the energy transfer mainly from mode (1, 1) upstream of 7 m. The growth rate curves intensively oscillate downstream x^* of 7.4 m. The mechanisms are different for mode (0, 2). $\sigma_{\mathcal{N}}$ of mode (0, 2) continuously decreases downstream x^* of 4.3 m. Instead, the linear mechanism is mainly responsible for the rapid amplification of mode (0, 2); in other words, mode

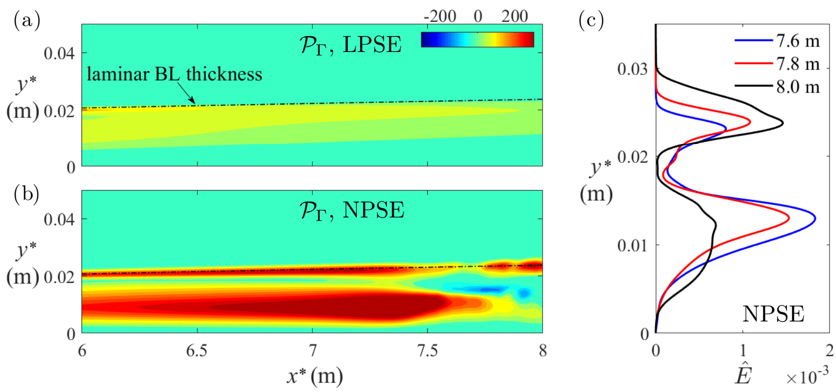

FIG. 16. Contribution density contours of the production term in (a) LPSE and (b) NPSE calculations, as well as (c) the disturbance energy profiles for mode (0, 2).

(0, 2) obtains energy mainly from the mean flow, rather than directly from mode (1, 1). This is consistent with the findings by Schmid and Henningson [46] for incompressible boundary layers. Zhang [47] also showed that the large amplitude of mode (0, 2) in hypersonic boundary layers was the result of the characteristics of its linear operator. Furthermore, $\sigma_{\mathcal{L}}$ obtained from NPSE is seen to be much larger than that from LPSE. This difference primarily comes from the production term, which means that the energy transfer from the mean flow to mode (0, 2) is strengthened at the presence of mode (1, 1) through the distortion of mode (0, 2) profile.

Figures 16(a) and 16(b) depict the spatial distribution of $\mathcal{P}_\Gamma$ of mode (0, 2) in the LPSE and NPSE cases. $\mathcal{P}_\Gamma$ from NPSE increases heavily in the middle and near the edge of the boundary layer, which is attributed to PU and PT, respectively. The disturbance energy profiles obtained from NPSE are plotted in Fig. 16(c) at different streamwise locations where nonlinear effects are significant. Two sharp peaks appear around the edge and in the middle of the boundary layer, respectively, strengthening the energy exchange between fluids in these two regions. More energy concentrates around the edge than in the middle as the profiles develop further downstream. The spatial distribution of mode (0, 2) discussed above might change with the vortex strength variation. This is checked by comparing the results with another two NPSE cases with $A^0_{(1,1)}$ of 0.5% and 0.005%, respectively, as shown in Fig. 17. The initial amplitude of mode (0, 2) rises by a factor of 100 when $A^0_{(1,1)}$ increases by 10, because its generation is due to nonlinear interaction. Nevertheless, the following growth of mode (0, 2) downstream is dominated by the linear mechanism in all the three cases with different $A^0_{(1,1)}$. Besides, the amplitudes of mode (0, 2) in the three cases all surpass mode (1, 1) further downstream. The contours of $\mathcal{P}_\Gamma$ of mode (0, 2) with different $A^0_{(1,1)}$ are plotted in Figs. 17(b) and 17(c) in the same style as Fig. 16(b). $\mathcal{P}_\Gamma$ from NPSE primarily distributes in the middle and near the edge of the boundary layer in both cases, which is shown to be insensitive to the vortex strength variation.

In the case with $A^0_{(1,1)}$ of 0.05%, the contours of $\mathcal{L}_\Gamma$ and $\mathcal{N}_\Gamma$ from NPSE for three typical modes, (1, 1), (2, 0), and (4, 4), are depicted in Fig. 18. The critical layer labeled is based on the phase speed of mode (1, 1). $\mathcal{L}_\Gamma$ concentrates between the critical layer and the boundary-layer edge when the disturbance is exponentially amplified, as discussed in Sec. III. When the nonlinear term becomes non-negligible, $\mathcal{L}_\Gamma$ gradually covers the entire boundary layer, including the near-wall region. This is attributed to the growth of the streamwise vortex modes, which distorted the mean flow profile. Besides, there are positive zones outside the laminar boundary layer downstream x^* of 7.5 m, increasing the transitional boundary-layer thickness. It is interesting to note that the contours of $\mathcal{N}_\Gamma$ bear strong resemblances to those of $\mathcal{L}_\Gamma$ downstream x^* of 7.3 m throughout the boundary layer, except for the opposite sign. This indicates that the intensive energy transfer among mode

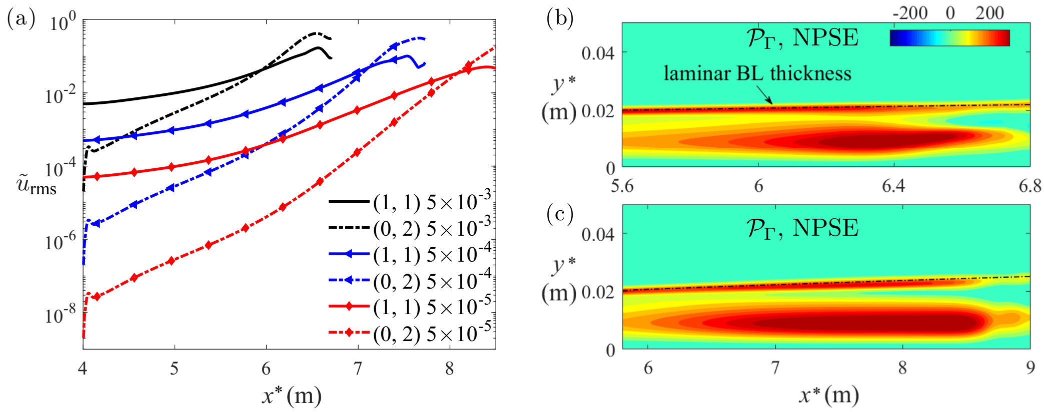

FIG. 17. (a) Streamwise distribution of the disturbance modes' amplitudes for cases with different $A^0_{(1,1)}$, as well as the contribution density contours of the production term in the NPSE cases of (b) $A^0_{(1,1)} = 0.5\%$ and (c) $A^0_{(1,1)}$ of 0.005%.

(1, 1) and others occurs where mode (1, 1) interacts strongly with the mean flow. This correlation between $\mathcal{L}_\Gamma$ and $\mathcal{N}_\Gamma$ also exists for other unsteady modes, such as modes (2, 0) and (4, 4) whose contours of $\mathcal{L}_\Gamma$ and $\mathcal{N}_\Gamma$ are plotted in Figs. 18(c)–18(f). It is concluded that when these unsteady modes are saturated in amplitudes, their primary role is to transfer the energy from their harmonic waves (or the mean flow) where they obtain the energy from the mean flow (or their harmonic waves).

Finally, the effect of the TCNE source term, $\mathcal{S}$, is studied in the disturbance nonlinear evolution with $A^0_{(1,1)}$ of 0.05%. Figure 19 plots the streamwise distribution of $\sigma_{\mathcal{S}}$ for the three selected modes. In the LPSE case, $\mathcal{S}$ is slightly stabilizing for all three modes. For modes (1, 1) and (2, 0), $\sigma_{\mathcal{S}}$ in the NPSE case follows the trace from LPSE downstream until x^* of 6.7 m, and then begins to oscillate. $\sigma_{\mathcal{S}}$ of mode (2, 0) is several times larger than that in the LPSE case downstream of saturation. However, the amplitude is still an order of magnitude smaller than the other terms. The streamwise-vortex mode (0, 2) is least affected by $\mathcal{S}$ in both the LPSE and NPSE cases. In the NPSE case, however, $\mathcal{S}$ is slightly destabilizing on mode (0, 2) though the growth rate is in the order of 0.01 /m.

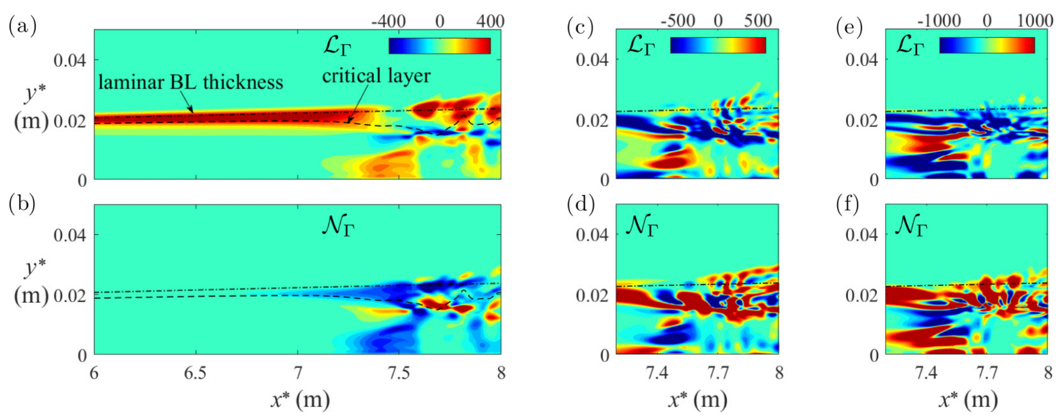

FIG. 18. Contribution density contours of the linear and nonlinear mechanisms, $\mathcal{L}_\Gamma$ and $\mathcal{N}_\Gamma$, for modes (1, 1) (a), (b), (2, 0) (c), (d), and (4, 4) (e), (f).

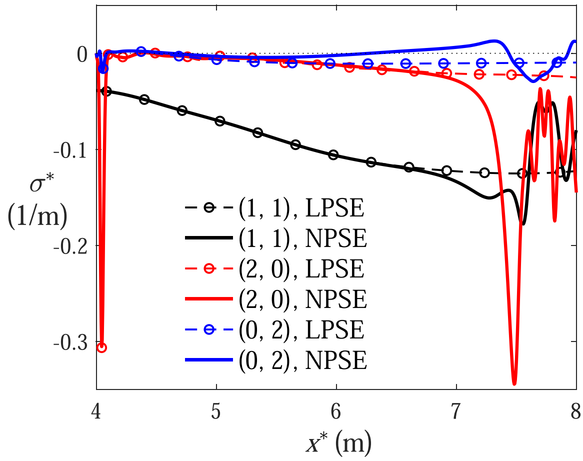

FIG. 19. Streamwise distribution of the TCNE source term σ_S for modes (1, 1), (2, 0), and (0, 2) in the LPSE and NPSE cases.

VI. CONCLUSIONS

In this study, the expression of the disturbance energy norm for TCNE flows is derived (see Sec. II D). According to it, we classify the terms in the governing equation of the disturbance energy: the production term is related to the energy exchange with the mean flow, the viscous term the dissipation and diffusion, the pressure work term the dilatation and diffusion, the TCNE source term the energy relaxation and species production/consumption, and the nonlinear term the energy exchange among different modes and the mean flow. Using both LST and PSE, the disturbance energy transfer mechanisms are explored in high-enthalpy boundary layers. In addition, the disturbance growth rate is decomposed to evaluate the contribution from each classified term [see Eq. (30)].

In the first-mode region, the growth rates are determined by the production term (destabilizing) and the viscous term (stabilizing), while the former nearly offset the latter. In the second-mode region, the viscous term decreases to the minimum, resulting in the dominance of the second mode. From the results with various spanwise wave numbers of disturbances, the production term causes the most unstable first-mode wave three-dimensional (see Fig. 7). The disturbance of the TCNE source term has a stabilizing effect on the second mode. It reduces the growth rate by at most 6% in the case of a Mach 10 adiabatic flat-plate flow with the highest free-stream temperature of 900 K. The pressure work term transfers energy from the middle of the boundary layer towards the wall. This positive contribution near the wall is strong and mainly comes from the dilatational pressure work, which is associated with the acoustic nature of the second mode between the wall and the sonic line. The contribution densities to the growth rate [see Eq. (29)] of both the production and viscous terms maximize near the critical layer. Moreover, their spatial distributions are similar among the cases with various T_∞^*, Ma_∞, and T_w^*, which reflects the universal characteristics of the energy transfer mechanisms. Compared with the results under the CPG assumption, the second mode is destabilized at a higher frequency in the TCNE case. The production term is mainly responsible for this difference in the second-mode growth rate, while the contribution from the disturbance of the TCNE source term is negligible. Therefore, TCNE changes the disturbance characteristics mainly through the mean flow modification.

The energy transfer mechanisms in the nonlinear disturbance evolution are studied through an oblique-mode breakdown case with initially a pair of oblique waves $(1, \pm 1)$. It is the linear mechanism, not the nonlinear one, that dominates the rapid amplification of the streamwise vortex mode (0, 2). In other words, the energy gain of mode (0, 2) comes much more from the mean flow than from mode (1, 1). Nevertheless, mode (1, 1) is found to strengthen the energy transfer from the mean flow to mode (0, 2) by the distortion of mode (0, 2) profile. This increase of the linear contribution density $\mathcal{L}_\Gamma$ primarily locates near the edge and in the middle of the boundary layer. This spatial distribution is shown to be insensitive to the vortex strength variation. When the harmonic waves are in comparable amplitudes with mode (1, 1), $\mathcal{L}_\Gamma$ gradually covers the whole boundary layer. For the unsteady modes, the contours of $\mathcal{N}_\Gamma$ bear strong resemblances to those of $\mathcal{L}_\Gamma$ with an opposite sign. This indicates that the intensive energy transfer between these modes and their harmonic waves occurs where they interact strongly with the mean flow. The streamwise-vortex mode is least affected by the TCNE source term $\mathcal{S}$. Although the stabilizing effect of $\mathcal{S}$ is several times stronger in the nonlinear regions, it is still an order of magnitude smaller than those of the production and viscous terms.

ACKNOWLEDGMENTS

This work was supported by the National Key Research and Development Plan of China through project No. 2019YFA0405201 and the National Key Project (Grant No. GJXM92579). The authors are also grateful for the support from National Science and Technology Major Project (2017-II-0004-0016), and NSFC Grants No. 92052103 and 12172195.

---

[1] M. V. Morkovin, Transition at hypersonic speeds, Tech. Rep., NASA Langley Research Center (1987).

[2] J. D. Anderson, Jr., *Hypersonic and High-Temperature Gas Dynamics*, 2nd ed. (AIAA, Reston, VA, 2006).

[3] P. A. Gnoffo, R. N. Gupta, and J. L. Shinn, Conservation equations and physical models for hypersonic air flows in thermal and chemical nonequilibrium, Tech. Rep., NASA Langley Research Center (1989).

[4] G. S. R. Sarma, Physico-chemical modelling in hypersonic flow simulation, Prog. Aerosp. Sci. **36**, 281 (2000).

[5] M. R. Malik and E. C. Anderson, Real gas effects on hypersonic boundary-layer stability, Phys. Fluids **3**, 803 (1991).

[6] C.-L. Chang, H. Vinh, and M. R. Malik, Hypersonic boundary-layer stability with chemical reactions using PSE, in *28th Fluid Dynamics Conference* (AIAA, Snowmass Village, CO, 1997).

[7] X. Chen, L. Wang, and S. Fu, Secondary instability of the hypersonic high-enthalpy boundary layers with thermal-chemical nonequilibrium effects, Phys. Fluids **33**, 034132 (2021).

[8] C. Kumar and A. Prakash, Secondary subharmonic instability of hypersonic boundary layer in thermo-chemical equilibrium over a flat plate, Phys. Fluids **33**, 024107 (2021).

[9] Y. Ma and X. Zhong, Receptivity to freestream disturbances of a Mach 10 nonequilibrium reacting oxygen flow over a flat plate, in *42nd AIAA Aerospace Sciences Meeting and Exhibit* (AIAA, Reno, Nevada, 2004).

[10] M. Di Renzo and J. Urzay, Direct numerical simulation of a hypersonic transitional boundary layer at suborbital enthalpies, J. Fluid Mech. **912**, A29 (2021).

[11] H. B. Johnson, T. G. Seipp, and G. V. Candler, Numerical study of hypersonic reacting boundary layer transition on cones, Phys. Fluids **10**, 2676 (1998).

[12] N. P. Bitter, Stability of hypervelocity boundary layers, Ph.D. thesis, California Institute of Technology (2015).

[13] C. H. Mortensen, Toward an understanding of supersonic modes in boundary-layer transition for hypersonic flow over blunt cones, J. Fluid Mech. **846**, 789 (2018).

[14] F. Miró Miró, E. S. Beyak, F. Pinna, and H. L. Reed, High-enthalpy models for boundary-layer stability and transition, Phys. Fluids **31**, 044101 (2019).

[15] O. Marxen, G. Iaccarino, and T. E. Magin, Direct numerical simulations of hypersonic boundary-layer transition with finite-rate chemistry, J. Fluid Mech. **755**, 35 (2014).

[16] P. J. Schmid and D. S. Henningson, *Stability and Transition in Shear Flows* (Springer, New York, 2001).

[17] B.-T. Chu, On the energy transfer to small disturbances in fluid flow (part I), Acta Mech. **1**, 215 (1965).

[18] K. J. George and R. I. Sujith, On Chu's disturbance energy, J. Sound Vib. **330**, 5280 (2011).

[19] A. Hanifi, P. J. Schmid, and D. S. Henningson, Transient growth in compressible boundary layer flow, Phys. Fluids **8**, 826 (1996).

[20] I. Padilla Montero and F. Pinna, Analysis of the instabilities induced by an isolated roughness element in a laminar high-speed boundary layer, J. Fluid Mech. **915**, A90 (2021).

[21] B. Saikia, S. M. Abdullah Al Hasnine, L. Dueñas, and C. Brehm, On the energy transfer mechanisms for the supersonic mode, in *AIAA Scitech 2021 Forum* (AIAA, Virtual Event, 2021).

[22] X. Chen, Y. Zhu, and C. Lee, Interactions between second mode and low-frequency waves in a hypersonic boundary layer, J. Fluid Mech. **820**, 693 (2017).

[23] C. Park, Assessment of two-temperature kinetic model for ionizing air, J. Thermophys. Heat Transfer **3**, 233 (1989).

[24] R. N. Gupta, J. M. Yos, and R. A. Thompson, A review of reaction rates and thermodynamic and transport properties for the 11-species air model for chemical and thermal nonequilibrium calculations to 30000 K, Tech. Rep., Scientific Research and Technology Inc. (1990).

[25] B. Bottin, D. V. Abeele, T. E. Magin, and P. Rini, Transport properties of collision-dominated dilute perfect gas mixtures at low pressures and high temperatures, Prog. Aerosp. Sci. **42**, 38 (2006).

[26] M. Capitelli, C. Gorse, S. Longo, and D. Giordano, Collision integrals of high-temperature air species, J. Thermophys. Heat Transfer **14**, 259 (2000).

[27] C. Park, *Nonequilibrium Hypersonic Aerothermodynamics* (John Wiley and Sons, New York, 1990).

[28] C. Park, R. L. Jaffe, and H. Partridge, Chemical-kinetic parameters of hyperbolic Earth entry, J. Thermophys. Heat Transfer **15**, 76 (2001).

[29] B. J. McBride, M. J. Zehe, and S. Gordon, NASA Glenn coefficients for calculating thermodynamic properties of individual species, Tech. Rep., NASA Glenn Research Center (2002).

[30] X. Chen and S. Fu, Convergence acceleration for high-order shock-fitting methods in hypersonic flow applications with efficient implicit time-stepping schemes, Comput. Fluids **210**, 104668 (2020).

[31] R. F. Probstein and D. Elliott, The transverse curvature effect in compressible axially symmetric laminar boundary-layer flow, J. Aeronaut. Sci. **23**, 208 (1956).

[32] F. G. Blottner, Chemical nonequilibrium boundary layer, J. Spacecr. Rockets **2**, 232 (1963).

[33] X. Chen, L. Wang, and S. Fu, Parabolized stability analysis of hypersonic thermal-chemical nonequilibrium boundary-layer flows, AIAA J. **59**, 2382 (2021).

[34] C.-L. Chang, Langley stability and transition analysis code (LASTRAC) version 1.2 user manual, Tech. Rep., NASA Langley Research Center (2004).

[35] M. L. Hudson, N. Chokani, and G. V. Candler, Linear stability of hypersonic flow in thermochemical nonequilibrium, AIAA J. **35**, 958 (1997).

[36] K. J. Franko, Linear and nonlinear processes in hypersonic boundary layer transition to turbulence, Ph.D. thesis, Stanford University, 2011.

[37] L. M. Mack, Boundary-layer linear stability theory, in *AGARD Special Course on Stability and Transition of Laminar Flow* (Jet Propulsion Laboratory, California Institute of Technology, 1984).

[38] Y. Zhu, C. Lee, X. Chen, J. Wu, S. Chen, and M. Gad-el Hak, Newly identified principle for aerodynamic heating in hypersonic flows, J. Fluid Mech. **855**, 152 (2018).

[39] F. P. Bertolotti, The influence of rotational and vibrational energy relaxation on boundary-layer stability, J. Fluid Mech. **372**, 93 (1998).

[40] C.-L. Chang, M. R. Malik, G. Erlebacher, and M. Y. Hussaini, Compressible stability of growing boundary layers using parabolized stability equations, in *22nd Fluid Dynamics, Plasma Dynamics and Lasers Conference* (AIAA, Honolulu, HI, 1991).

[41] N. P. Bitter and J. E. Shepherd, Stability of highly cooled hypervelocity boundary layers, J. Fluid Mech. **778**, 586 (2015).

[42] C. D. Pruett and C.-L. Chang, Spatial direct numerical simulation of high-speed boundary-layer flows part II: Transition on a cone in Mach 8 flow, Theor. Comput. Fluid Dyn. **7**, 397 (1995).

[43] K. J. Franko and S. K. Lele, Breakdown mechanisms and heat transfer overshoot in hypersonic zero pressure gradient boundary layers, J. Fluid Mech. **730**, 491 (2013).

[44] C. S. J. Mayer, D. A. Von Terzi, and H. F. Fasel, Direct numerical simulation of complete transition to turbulence via oblique breakdown at Mach 3, J. Fluid Mech. **674**, 5 (2011).

[45] J. Sivasubramanian and H. F. Fasel, Direct numerical simulation of transition in a sharp cone boundary layer at Mach 6: Fundamental breakdown, J. Fluid Mech. **768**, 175 (2015).

[46] P. J. Schmid and D. S. Henningson, A new mechanism for rapid transition involving a pair of oblique waves, Phys. Fluids **4**, 1986 (1992).

[47] C. Zhang, Research on nonlinear mode interactions relating to supersonic boundary layer transition (in Chinese), Ph.D. thesis, Tianjin University, 2017.